Award Number: W81XWH-09-2-0016

TITLE: Biomechanics of Head, Neck, and Chest Injury Prevention for Soldiers

PRINCIPAL INVESTIGATOR: Dr. Stefan Duma

CONTRACTING ORGANIZATION: Virginia Polytechnic Institute and State University
Blacksburg, VA 24060

REPORT DATE: March 2011

TYPE OF REPORT: Final

PREPARED FOR: U.S. Army Medical Research and Materiel Command
Fort Detrick, Maryland 21702-5012

REPORT DOCUMENTATION PAGE

Form Approved
OMB No. 0704-0188

1. REPORT DATE *(DD-MM-YYYY)*	**2. REPORT TYPE**	**3. DATES COVERED** *(From - To)*
01-03-2011	Final	1 MAR 2009 - 28 FEB 2011

4. TITLE AND SUBTITLE

Biomechanics of Head, Neck, and Chest Injury Prevention for Soldiers

5a. CONTRACT NUMBER

5b. GRANT NUMBER
W81XWH-09-2-0016

5c. PROGRAM ELEMENT NUMBER

6. AUTHOR(S)

Dr. Stefan Duma

E-Mail: duma@vt.edu

5d. PROJECT NUMBER

5e. TASK NUMBER

5f. WORK UNIT NUMBER

7. PERFORMING ORGANIZATION NAME(S) AND ADDRESS(ES)

Virginia Polytechnic Institute and State University
Blacksburg, VA 24060

8. PERFORMING ORGANIZATION REPORT NUMBER

9. SPONSORING / MONITORING AGENCY NAME(S) AND ADDRESS(ES)

U.S. Army Medical Research and Materiel Command
Fort Detrick, Maryland 21702-5012

10. SPONSOR/MONITOR'S ACRONYM(S)

11. SPONSOR/MONITOR'S REPORT NUMBER(S)

12. DISTRIBUTION / AVAILABILITY STATEMENT

Approved for Public Release; Distribution Unlimited

13. SUPPLEMENTARY NOTES

14. ABSTRACT

No abstract provided.

15. SUBJECT TERMS

No subject terms provided.

16. SECURITY CLASSIFICATION OF:			**17. LIMITATION OF ABSTRACT**	**18. NUMBER OF PAGES**	**19a. NAME OF RESPONSIBLE PERSON**
a. REPORT	**b. ABSTRACT**	**c. THIS PAGE**			USAMRMC
U	U	U	UU	39	**19b. TELEPHONE NUMBER** *(include area code)*

Virginia Tech - Wake Forest
Center for Injury Biomechanics

www.cib.vt.edu

CIB Report Number 2011-011

Final Report: Phase 1 Biomechanics of Head, Neck, and Chest Injury Prevention for Soldiers

PREPARED FOR

Mr. Frederick Brozoski
U.S. Army Aeromedical Research Laboratory
6901 Farrell Road
Ft. Rucker, AL 36362
Phone: 334-255-6881
Fax: 334-255-7798

PREPARED BY

Steve Rowson, Stefan Duma, Joel Stitzel, Joe Cormier,
Warren Hardy, and Clay Gabler
Center for Injury Biomechanics
439 ICTAS Building, Stanger St
Blacksburg, VA 24061
Phone: 540-231-1617 Fax: 540-231-2953
duma@vt.edu

June 2011

EXECUTIVE SUMMARY

This is the final report for Phase 1 of the cooperative agreement between the Virginia Tech – Wake Forest, Center of Injury Biomechanics and the U.S. Army entitled "Biomechanics of Head, Neck, and Chest Injury Prevention for Soldiers." The final report includes activities performed during the entire Phase 1 timeline, which can be seen in Figure 1. Task 1 details facial fracture prediction using the Facial and Ocular CountermeasUre Safety (FOCUS) with risk functions for the frontal bone, maxilla, and nasal bone. For Task 2, development of CAD data for biomechanical studies of the cervical spine is provided in place the head supported mass analysis (Task 2.1/2.2), as agreed upon with USAARL. Task 3 includes the finite element model of the lung and injury criteria development (3.1), development of a head surrogate for free field blast testing (3.2, as agreed upon with USAARL), and crash sled system development for thorax injury protection (3.3). The National Research Symposium on Military Biomechanics (4.1) is also reported on. All tasks for Phase 1 have been completed by the end of the 2 year project term.

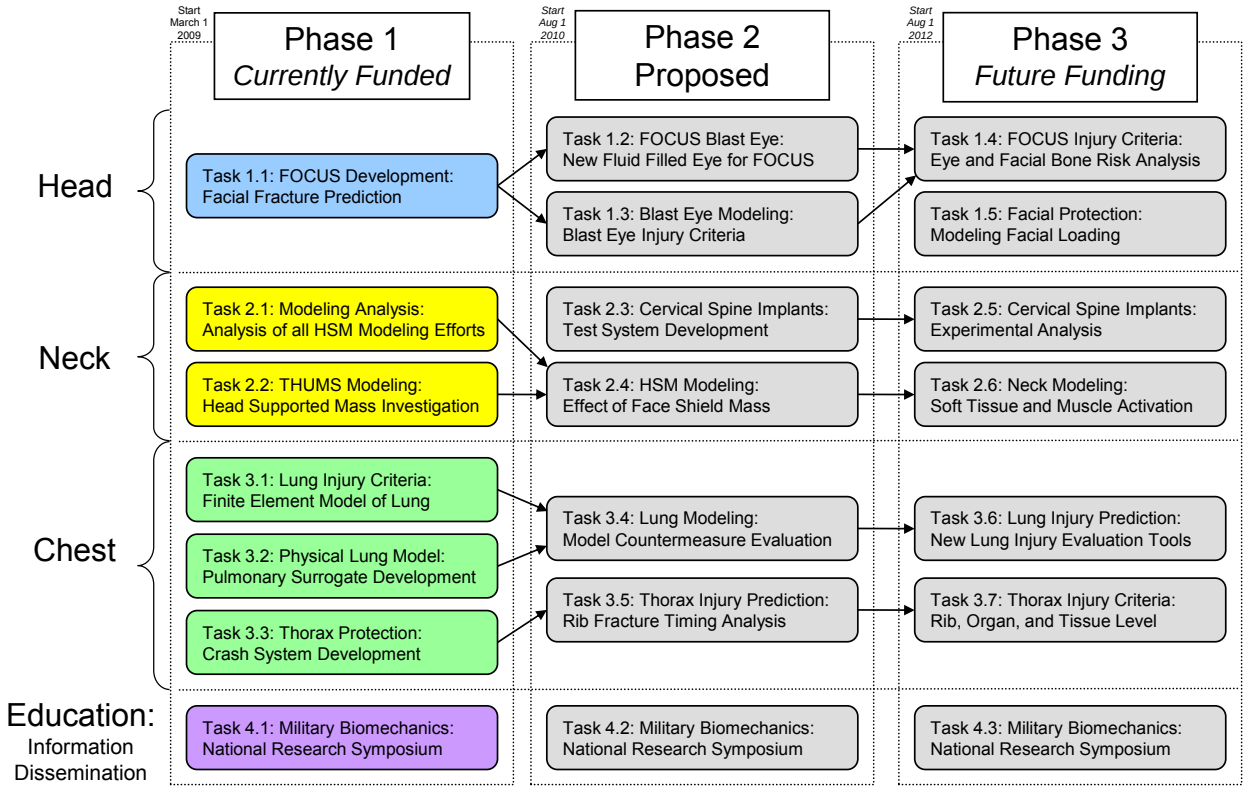

Figure 1: Biomechanics of head, neck, and chest injury prevention research outline. This final report covers all Phase 1 activities (highlighted).

Task 1.1: FOCUS Development – Facial Fracture Prediction

Specific Objectives of Task 1.1:

1. Determine the biofidelity corridors for the FOCUS head form facial response based on experimental frontal impact tests
2. Analyze the published injury threshold data to create the human corridors
3. Derive a scaling function between the human corridors and the FOCUS load measurements for frontal impact facial fracture prediction

Fracture of the facial bones can be devastating to the facial structures and can be associated with injuries such as brain or ocular injuries. In the past, there has been little work focusing on facial fracture research and therefore, there is a lack of detailed information necessary to determine the force at which a given facial bone is expected to fracture. Facial bone tolerance has been investigated by several researchers using a variety of methods. Despite these efforts, a clear understanding of facial tolerance has yet to be defined. The purpose of this study is analyzing data from an existing series of tests on the frontal, nasal and maxilla in order to develop a statistical relationship between impactor force and the risk of fracture. In addition, a series of drop tests are performed on the FOCUS head to evaluate its biofidelity.

The data for this study were obtained from existing data that included facial impacts on male cadaveric subjects. The methods of that study consisted of striking the facial bones of 31 subjects with the flat face (area = 6.45 cm^2) of an unpadded, cylindrical impactor (3.2 kg), along with the use of acoustic emission sensors to determine the time of fracture onset. Each head was rigidly mounted to a semi-circular polycarbonate support using Bondo. Specific anatomical landmarks were used to determine impact location. For frontal bone impacts, the impactor was positioned such that its lower edge was centered to the orbit and superior to the superciliary arch. For nasal bone impacts, the impactor was centered over the palpated inferior surface of the nasal bone. For maxilla impacts the impactor was aligned vertically below the center of the orbit at a level such that the top of the impactor was just below the inferior orbital rim. The rigid impactor was instrumented with two single-axis accelerometers (Endevco 7264B-2000, Endevco Corp., San Juan Capistrano CA). A load cell (Denton, 8617JTF, Rochester Hills, MI) was attached to the tip of the impactor which was also instrumented with a single axis accelerometer (Endevco 7264B-2000, Endevco Corp., San Juan Capistrano CA).

In all cases an AE sensor (Micro30S, Physical Instruments, New Jersey) was mounted to the frontal bone, just posterior to the apex of the forehead. The AE sensor was mounted directly to the bone by removing the soft tissue and periosteum and gluing the sensor in place with cyanoacrylate adhesive. Additionally, high-speed video was also recorded at a frame rate of approximately 4,000 fps. Impactor displacement calculated by double integrating impactor acceleration was verified using high-speed video analysis. To define the average force-displacement response of each bone, a corridor was created to encompass the overall force-displacement response.

A series of impacts were performed on corresponding regions of the Facial and Ocular CountermeasUre for Safety (FOCUS) headform (Figure 2) in order to characterize its response to blunt impact (Figure 3). The impact severity was chosen to facilitate comparison with the previous study cadaver results and to minimize risk of damaging the headform. The impact was applied using the same apparatus and instrumentation scheme used for the cadaver impacts. The stiffness of the FOCUS response was determined up to 20% and between 20% and 80% of the peak force for comparison to the cadaveric response. This separation was chosen to provide a more realistic description of the force-displacement response, which consisted of a softer toe region.

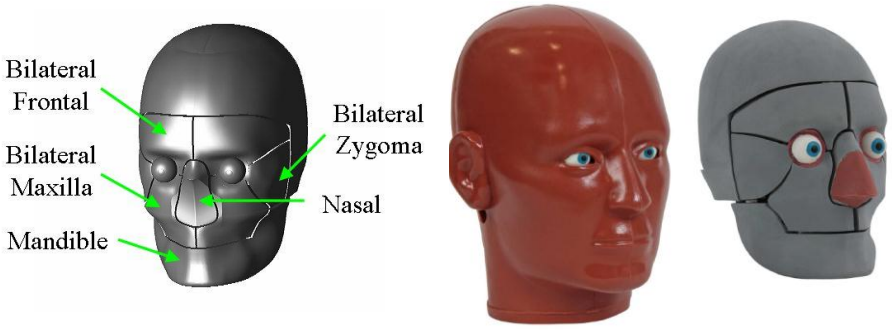

Figure 2: Load cell locations in FOCUS headform (left), assembled headform with skin (center) and without skin.

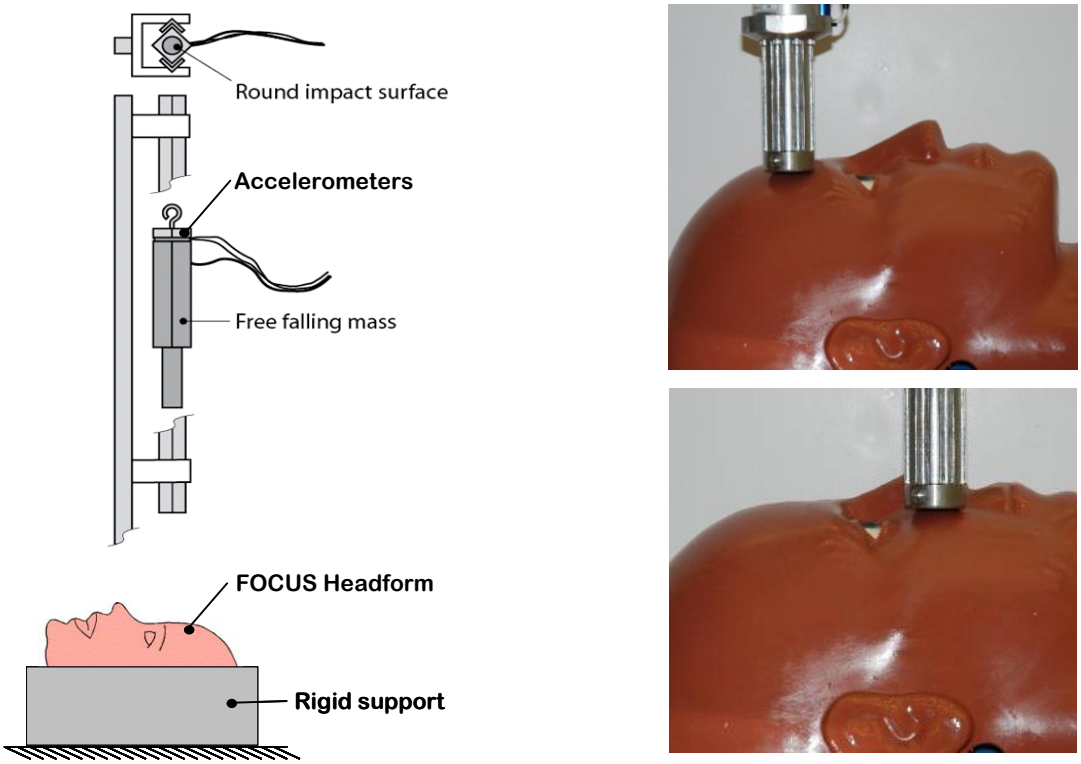

Figure 3: Schematic of drop tower used to measure FOCUS force-deflection response (left), impact location for frontal bone (top right), and impact location for maxilla (bottom right).

The results of this study include an understanding of the tolerance of the facial bones and the biofidelity of the FOCUS headform. Statistical analyses were performed using parametric and non-parametric techniques to estimate the risk of fracture as a function of impactor force. This is the first study to produce such a relationship due to the previous lack of available data. For the frontal bone, the results of this study suggest that a 50% risk of fracture occurs at 1885 to 2405 N (Figure 4). For the nasal bone, the 50% risk of fracture occurred at a force between 450 to 850 N (Figure 5). For the maxilla impacts, a 50% risk of fracture occurred a force between 1,140 to 1,220 N (Figure 6). The risk functions developed in this study can be used in conjunction with the FOCUS headform in order to assess the risk of facial fracture utilizing its internal load cells.

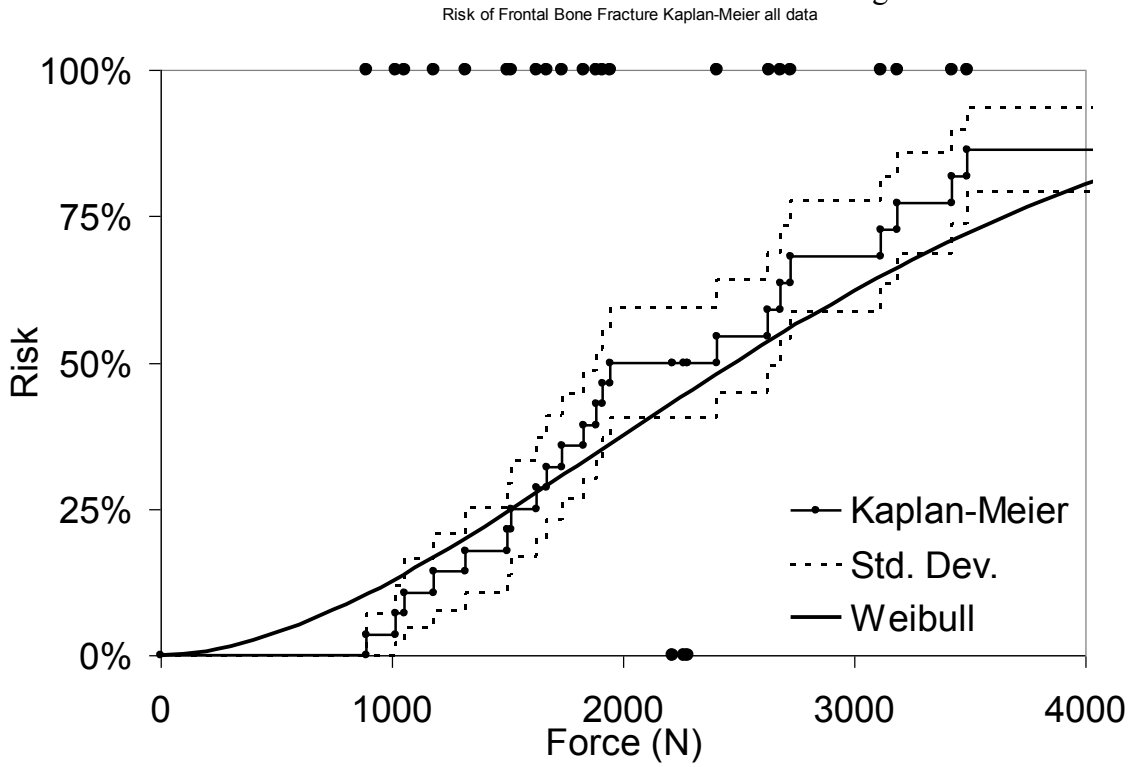

Figure 4: Parametric and non-parametric injury risk functions for the frontal bone. A force between 1885 and 2405 N represents 50% risk of fracture.

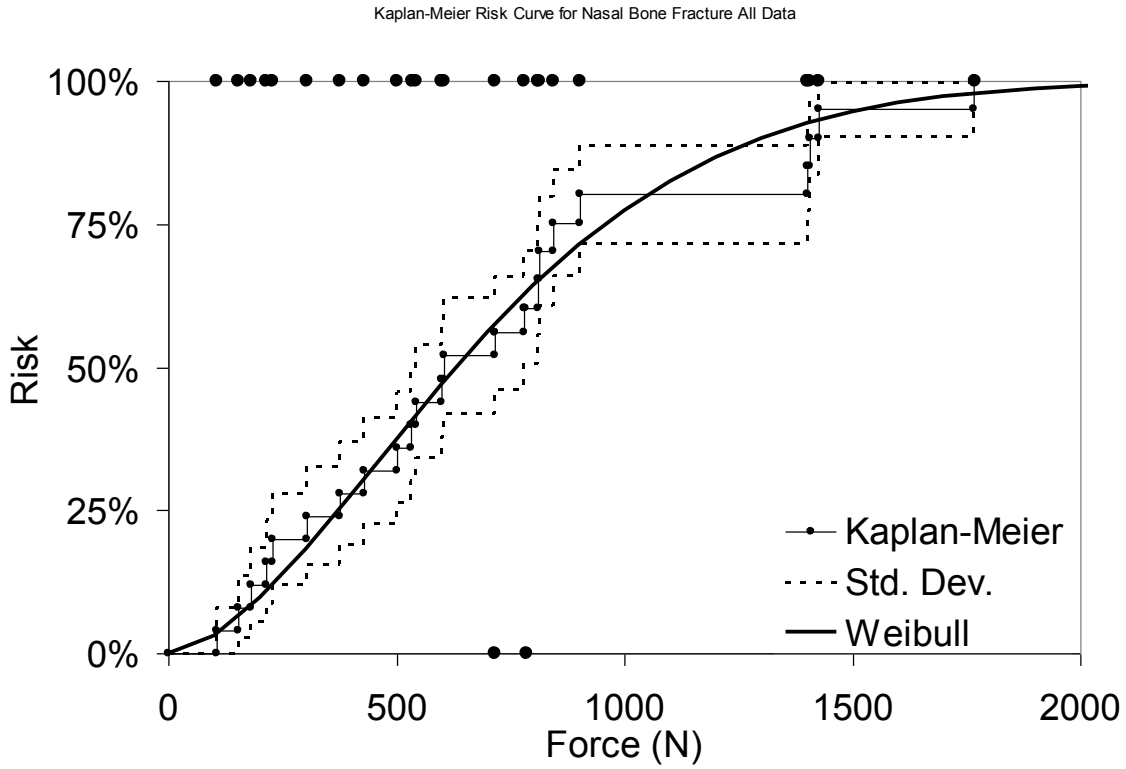

Figure 5: Parametric and non-parametric injury risk functions for the nasal bone. A force between 450 and 850 N represents 50% risk of fracture.

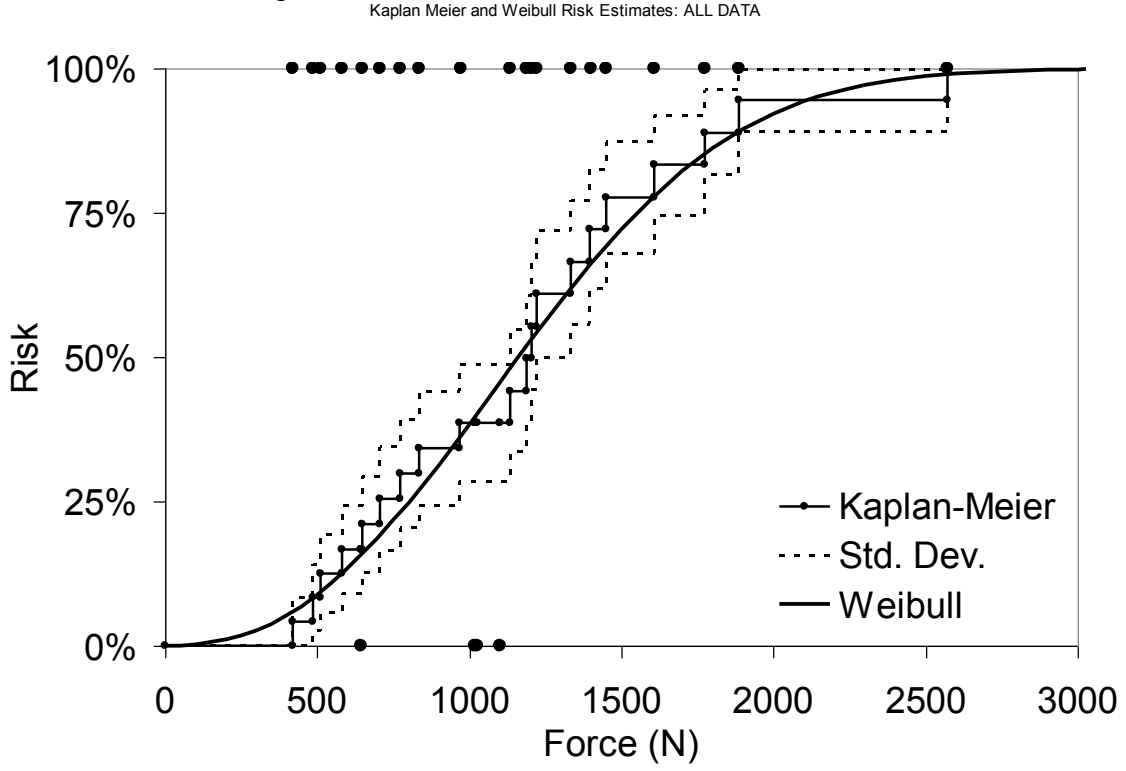

Figure 6: Parametric and non-parametric injury risk functions for the maxilla. A force between 1,140 and 1220 N represents 50% risk of fracture.

Additionally, the average force-displacement response (stiffness) of the cadaver and FOCUS was created using the characteristic average to facilitate comparison. The data suggest that for impacts to the frontal and maxilla regions, the FOCUS headform is expected to produce similar forces to those of the cadaver subjects (Figure 7). Due to variation in the geometrical characteristics of the cadaver subjects a wide range in force-displacement response was observed for the nasal impacts. The sensitivity of the nasal bone region of the FOCUS headform to impacts of various regions was also demonstrated. Overall, the FOCUS headform was repeatable at every impact location, producing a similar response between each test.

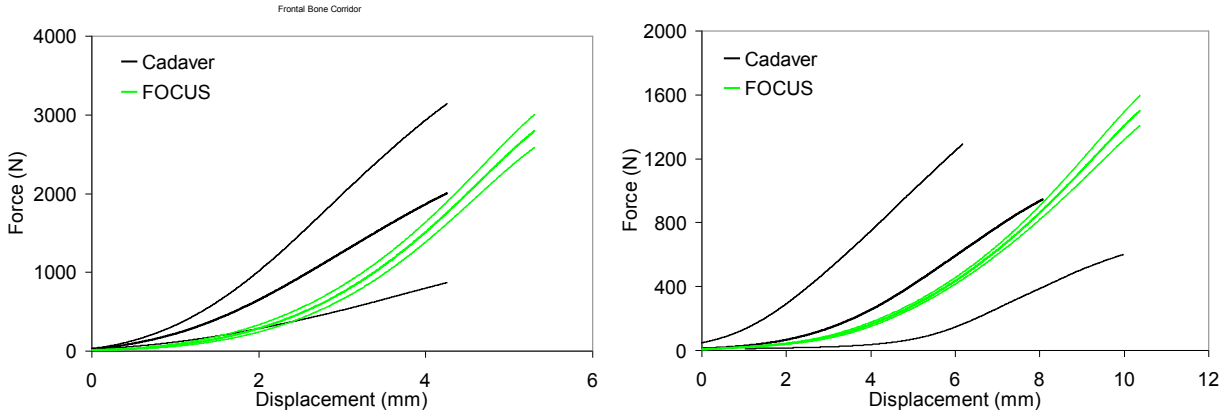

Figure 7: Force deflection plots comparing previous cadaver data to FOCUS data for the frontal bone (left) and maxilla bone (right).

In summary, the results of this study provide knowledge that can be used to assess the risk of frontal, nasal and maxilla fractures. The force-displacement corridors developed in this study demonstrate the biofidelity of the FOCUS headform which can be used to improve its capabilities in the future and aid in the development of additional surrogates used to investigate facial injuries.

Tasks 2.1/2.2: Development of CAD Data for Biomechanical Studies of the Cervical Spine

Based on discussions with USAARL, the modeling analysis of head supported mass, THUMS HSM studies, and studies of face shield mass effect on neck injury biomechanics (Tasks 2.1 and 2.2) have been replaced with efforts to support cervical spine implant modeling and neck model development. Results of this development are shown below.

A novel approach to CAD model development based on a single living subject, scanned in multiple modalities and postures was used to complete this work. Given the amount of data that is required for model reconstruction, there is not one single imaging modality would provide all the data necessary to construct a biofidelic model of the neck and cervical spine. Instead, we applied a multi-modality scanning protocol including MRI, upright MRI, CT, as well as methods for external anthropometry data collection. We aimed to improve upon previous model development efforts by acquiring and using scans where the participant is seated upright, and in the correct orientation with gravity. A healthy male subject, aged 26 years was used as the framework of the model. This individual met selection criteria after extensive pre-screening. His height, weight, and BMI were 174.9 cm, 78.6 ± 0.77 kg, and 25.7 respectively. Fifteen anthropometric measurements were taken in both seated and standing positions and showed excellent agreement (Gordon, Churchill et al. 1989; Gayzik, Hamilton et al. 2009). An overview of the data collected is shown in Figure 8.

A. B. C.

Figure 8: Data acquired for neck model construction. Left, 3D reconstruction of upright neck MRI scan. Middle, external anthropometry collection on average male subject in the seated position. Right, overlap of CAD anatomy (red outline) on a single upright MRI image taken through the sagittal plane.

The subject underwent the following image data collection protocol (Gayzik, Hamilton et al. 2009). MRI image data with the participant in the supine position was collected on a 1.5 Tesla TwinSpeed MRI scanner (GE, Milwaukee, WI). The pulse sequence was selected to accentuate borders of fat and water (muscle, organ, etc.). The upright MRI protocol utilized a 0.6 T Fonar Upright MRI (Fonar Inc., Melville, NY). Three dimensional gradient echo pulse sequences similar to those developed for the close-bore MRI scanner were used so that the resulting images were acquired with the fat and water signal out of phase (Figure 8C). Computed tomography (CT) scans were acquired from the study subject using a GE LightSpeed, 16-slice scanner.

Images were acquired in helical mode, with the subject in the supine and an approximately seated position. Model construction relied on extensive external anthropometry data collected from the participant. Data were collected with a 7-axis 3D digitizer (Faro, Platinum Model arm, 8 ft. (2.4 m), Lake Mary, FL). We collected data from the subject in the seated position. Images from the upright scans were combined to form regional image sets used in the model assembly (Figure 2).

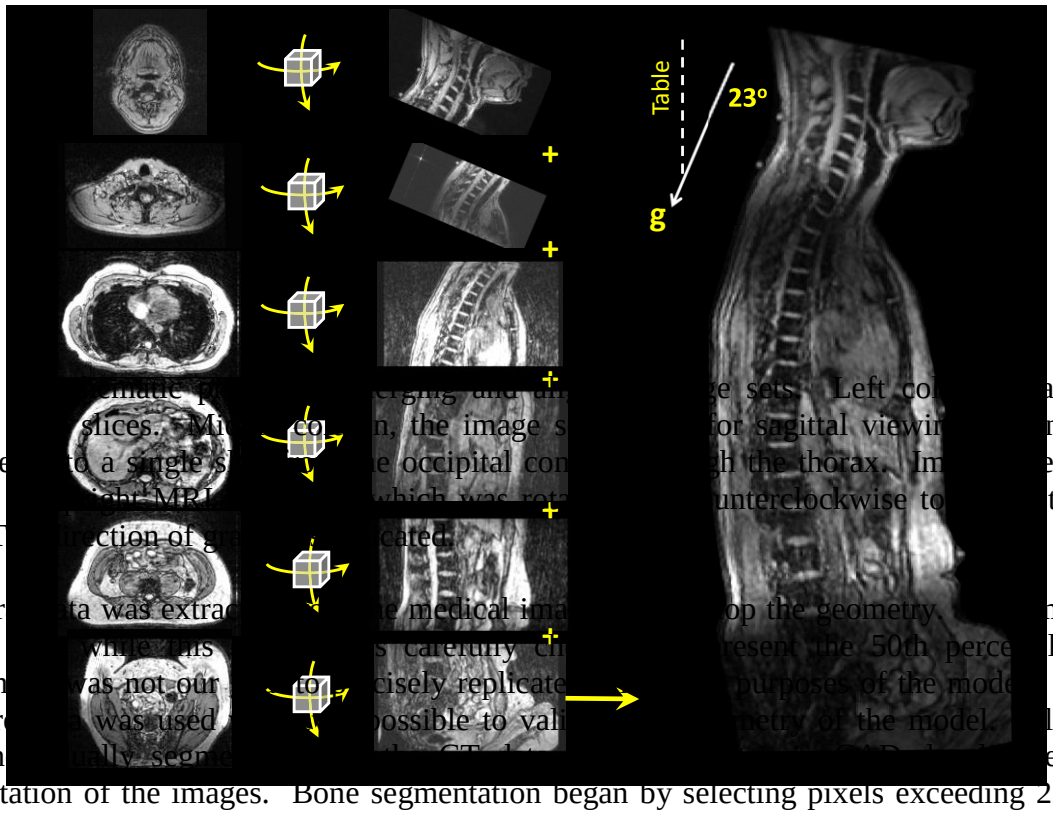

Figure [illegible] ge sets. Left col[illegible]ansverse upright [illegible] slices. Mi[illegible]co[illegible]n, the image s[illegible]for sagittal viewin[illegible]ns were combine[illegible]o a single s[illegible]e occipital con[illegible]gh the thorax. Im[illegible]e shown relative [illegible]ight MRI [illegible]which was rot[illegible]unterclockwise to [illegible]the seat buck. T[illegible]ection of g[illegible]cated.

Structur[illegible]ta was extrac[illegible]e medical ima[illegible]op the geometry. [illegible]nportant to note [illegible]while this [illegible]s carefully ch[illegible]resent the 50th perce[illegible]le male occupan[illegible]was not our [illegible]to [illegible]cisely replicate [illegible]purposes of the mode[illegible] Instead literatur[illegible] was used [illegible]possible to val[illegible]metry of the model. [illegible]ll bones were in[illegible]ally segm[illegible]CT data[illegible]ent was segmentation of the images. Bone segmentation began by selecting pixels exceeding 226 HU. To assist in determining cortex edges, a gradient magnitude filter was applied to the images. Bones with small articular spaces (such as cervical vertebra) were manually separated. The polygon surfaces were conditioned to remove artifacts and any structural abnormalities that were found in the resulting segmentations. The segmentation and conditioning process for a sample bone is shown in Figure 10. For many of the bones along the axial skeleton, symmetry was enforced. A least squares fit plane through the polygon data was used to mirror the object (Figure 10B). Following the mirroring process, deviations from the original segmented polygon were conducted to verify that significant structural changes had not been introduced in this process (Figure 10C).

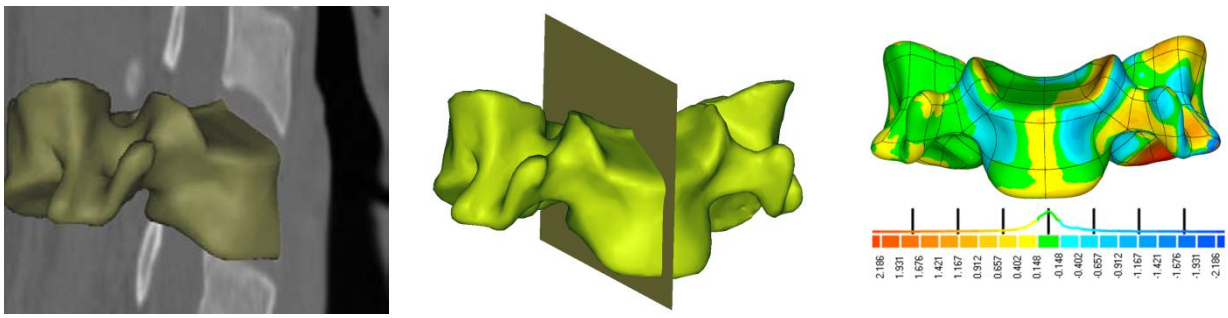

A. B. C.

Figure 10: Bone segmentation and conditioning process. A. Bone (C5) from segmentation, B. C5, with symmetry plane fit, C. C5, mirrored, showing deviations from original segmentation (Units: mm).

Muscles were segmented for the model development effort as were germane to modeling neck kinematics. In each body region, muscles were directly segmented from the supine MRI image data using dynamic region growing, multi-slice editing, and morphological operations (Mimics v 14, Leuven, Belgium). The selection of the FSPGR (Fast Spoiled Gradient Recalled) pulse sequence, i.e. imaging fat and water out of phase, was especially well suited for segmenting large muscle groups since in many cases a clear outline was visible. Fifty-two muscles of the neck were explicitly segmented. This included 26 muscles on each side, with the only grouped muscles being sternothyroid and thyrohyoid. Most tendinous muscle attachments in this region were not segmentable due to their thin cross-section and low water content (Gray 1918). In these cases classical anatomical texts were used to determine muscle attachment locations and 3D polygon models were modified accordingly in the conditioning phase. In some cases, neck muscles segmentation was not possible using the 1.5 T scans of the neck. In these cases, we referred to high-resolution digitized photographs of anatomical cross sections of the Visible Human Project to determine muscle course and attachment locations (Spitzer, Ackerman et al. 1996). A 3D rendering of the segmented neck musculature is shown in Figure 11.

Figure 11: Three dimensional rendering of neck musculature CAD data.

Careful attention was given to anatomically accurate insertion and origin points on the bony skeleton for these neck muscles. Attachments sites were determined by Boolean subtraction with bones. Neck muscle volumes compared well to previous literature studies (Figure 12 and Figure 13) (Knaub, Van Ee et al. 1998; Hedenstierna and Halldin 2008). Origin and insertion points of the neck muscles are dispersed throughout neighboring body regions and can be found on the

skull, cervical spine, thoracic spine, rib cage, and scapula. Soft tissue data segmented in MRI scans were transformed to the model coordinate system using landmarks on bones.

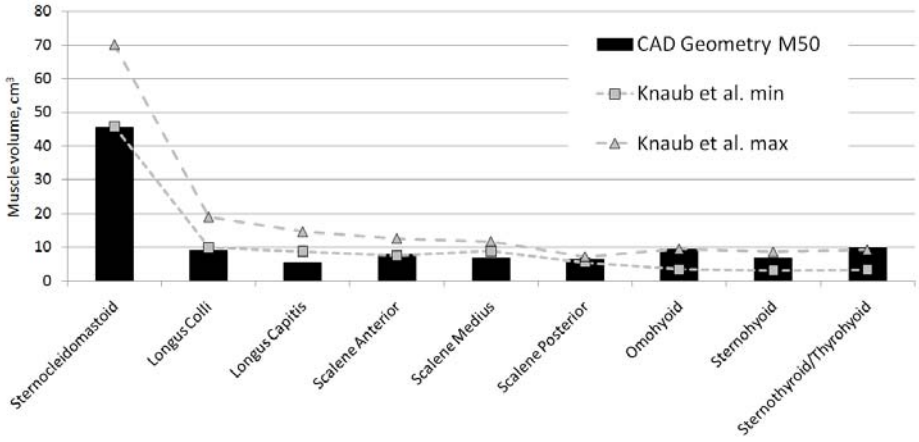

Figure 12: Anterior muscle volumes of the neck, as compared to Knaub et al.

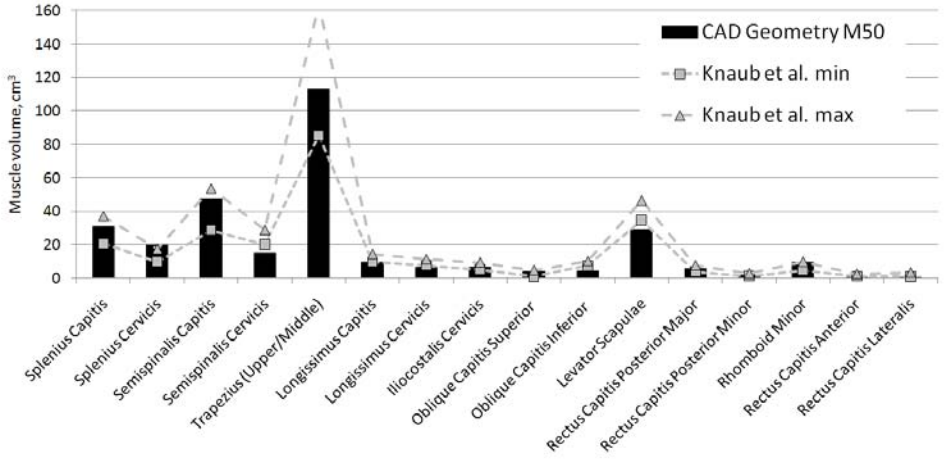

Figure 13: Posterior and lateral muscle volumes of the neck, as compared to Knaub et al.

The final stage of model development was the CAD development. Here, the conditioned polygon data was converted to a mathematically defined NURBS patchwork. There are a number of key elements in this conversion. The first process (data conditioning) was described in the previous section on bone. A preliminary patchwork was constructed on the conditioned polygon surfaces obtained through segmentation. The patchwork was further refined to strike a balance between computational efficiency and resolution. Border continuity was enforced such that the patchwork was G1 continuous, meaning that the first derivative of each patch is continuous with neighboring patches. If sagittal symmetry was required for a given part, the patch work was completed on one half of the part and then mirrored. Given the amount of parts in the complete model, care was taken to use the appropriate resolution for the surface patches. The least amount of isoparms (splines) per patch that still captured the contours of the underlying polygon model was used in all cases.

CAD data has been developed for the following structures in the neck. Cervical vertebrae 1 through 7, the hyoid bone, the C2 cartilage, spinal cord, 52 muscles of the neck (listed in Figure 12 and Figure 13), the thyroid, and cricoid cartilage surfaces as well as the trachea (See Figure 14). Disk geometry can be readily determined from the cervical vertebral bodies. A soft tissue structure representing fascia and skin has been developed from CT scans and external anthropometry scans (See Figure 15). Structures describing the thoracic bony anatomy (T1, first rib, clavicle) were constructed in order to accurately portray the insertions and origins of musculature. In addition to the muscle volumes (Figure 12 and Figure 13 above), several other aspects of the model geometry have been validated against literature values. The overall curvature of the neck matches typical curvature per the work of Klinich et al. (Klinich, Ebert et al. 2004). In addition the facet spacing of the spine was validated against work by Yoganandan et al. (Yoganandan, Knowles et al. 2003).

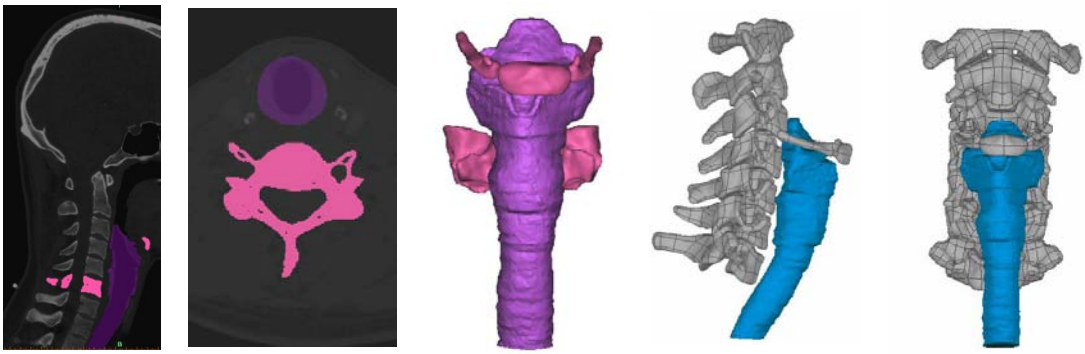

A. B. C. D. E.

Figure 14: CAD development process of anterior airway soft tissue structures in the neck. A. Sagittal view, segmentation from CT data. B. Transverse view CT data. C. Segmented data (purple) with bones used in transformation from CT to model space. D. Lateral view of additional airway soft tissue with CAD data. E. Anterior view of airway soft tissue.

In summary, the CAD model presented contains adequate detail for injury biomechanics investigations of the cervical spine. Based on the following merits, it is well suited for cervical implant investigations: the geometry has been shown to match literature cases for curvature and cervical vertebral body spacing, the source data was taken in an upright position, the source data was acquired from a living and healthy subject, and the subject was found to represent the average male based on available data from a military population.

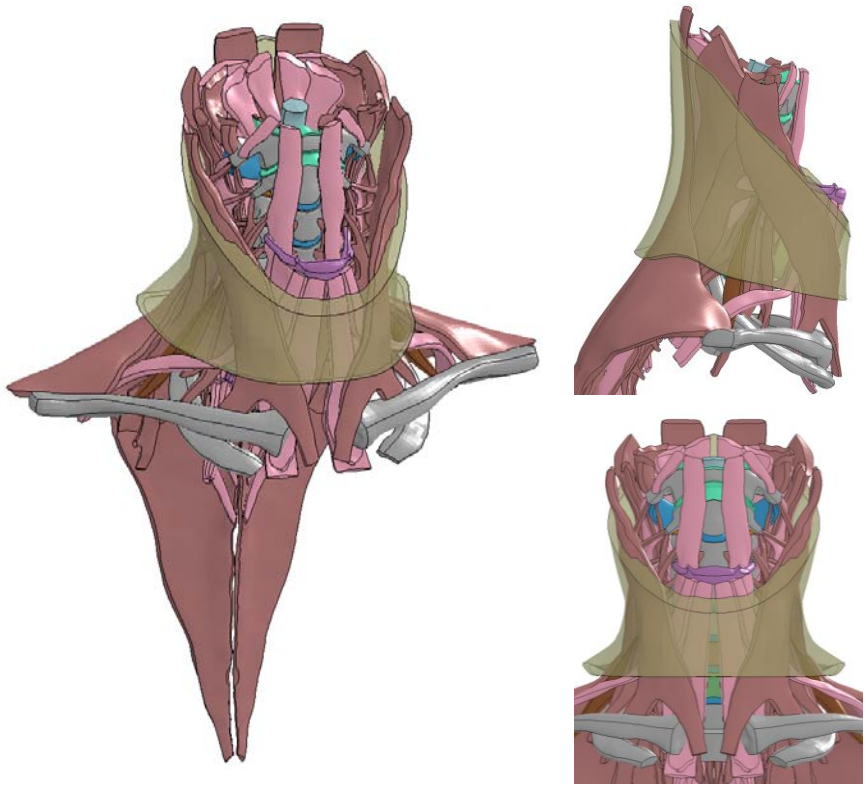

Figure 15: Oblique, lateral and anterior view of the soft tissue neck model.

References

Gayzik, F., C. Hamilton, et al. (2009). Multi-Modality Image Data Collection Protocol for Full Body Finite Element Model Development. SAE Digital Human Modeling. Gothenburg, Sweden, SAE.

Gordon, C., T. Churchill, et al. (1989). 1988 Anthropometric Survey of U.S. Army Personnel: Methods and Summary Statistics. D. a. E. C. Prepared for United States Army Natick Research.

Gray, H. (1918). Anatomy of the Human Body, Lea & Febiger.

Hedenstierna, S. and P. Halldin (2008). "How does a three-dimensional continuum muscle model affect the kinematics and muscle strains of a finite element neck model compared to a discrete muscle model in rear-end, frontal, and lateral impacts." Spine (Phila Pa 1976) 33(8): E236-45.

Klinich, K., S. Ebert, et al. (2004). "Cervical Spine Geometry in the Automotive Seated Posture: Variations with Age, Stature, and Gender." Stapp Car Crash J 48: 301-330.

Knaub, K., C. Van Ee, et al. (1998). Measurement of Human Neck Muscle Volume Geometry and Physiologic Cross Sectional Area in 5th, 50th, and 95th Percentile Subjects Using Cadaveric Dissection and MRI. NHTSA.

Spitzer, V., M. Ackerman, et al. (1996). "The Visible Human Male: A Technical Report." JAMIA 3: 118-130.

Yoganandan, N., S. A. Knowles, et al. (2003). "Anatomic study of the morphology of human cervical facet joint." Spine (Phila Pa 1976) 28(20): 2317-23.

Task 3.1: Lung Injury Criteria: Finite Element Model of Lung

Specific Objectives of Task 3.1:

1. Develop a finite element model of the lung capable of predicting contusions
2. Establish lung injury criteria

Lung injury is prevalent in the civilian population due to vehicle crash. It is an injury that is also experienced in-theater through behind armor blunt trauma, or blast loading. Although the loading rate for these injuries can differ substantially, computational modeling can be an effective tool to investigate novel countermeasures for pulmonary injury. We have developed accurate computational geometry models for targeted anatomy, based on multi-modality image segmentation. Here, we focus on how this approach was used for the development of thoracic anatomy, including key anatomical detail while accounting for postural changes.

Living subjects were used to collect soft tissue and skeletal anatomical image data. The 50th percentile male model is based on an individual with height, weight, and BMI of 174.9 cm, 78.6 ± 0.77 kg, and 25.7 respectively. Individuals were also recruited for the female 5th and 50th percentiles, and the male 95th percentile.

The subjects underwent an imaging protocol consisting of both supine and upright Magnetic Resonance Imaging (MRI), Computed Tomography (CT), and external body scanning, Figure 16. (Gayzik, Hamilton et al. 2009) The resulting images were used synergistically, along with supplemental data sources, to create CAD models. The assembly phase involved repositioning segmentations to align with images taken in an upright and seated posture. NURBS (non-uniform rational b-spine) surfaces were overlaid onto the polygon data extracted from the images to create the final geometry.

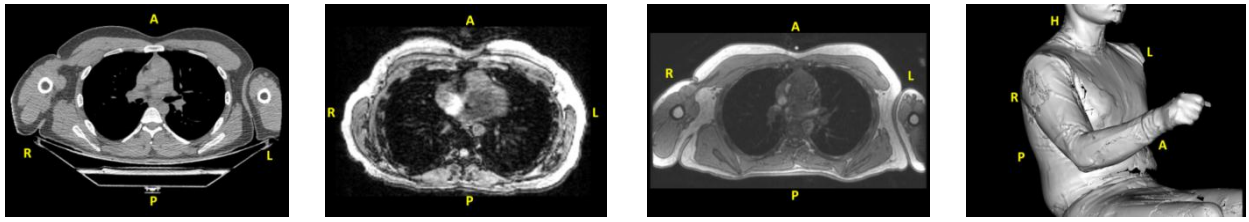

A. B. C. D.

Figure 16: Overview of data collected for full body CAD development, showing examples of thorax data. A. Conventional MRI, supine, B. Upright MRI, C. CT, supine, D. External body laser scan (raw point data).

The M50 CAD exhibits all necessary aspects for thoracic biomechanical modeling efforts. The model is composed of mathematical surfaces that are G1-continuous and water-tight to a tolerance of 0.01 mm. The thorax model consists of all bones, heart, lungs, great vessels, pectoral muscles, deltoids, as well as large upper extremity muscles. The size, volume and morphology of these models represent the average male.

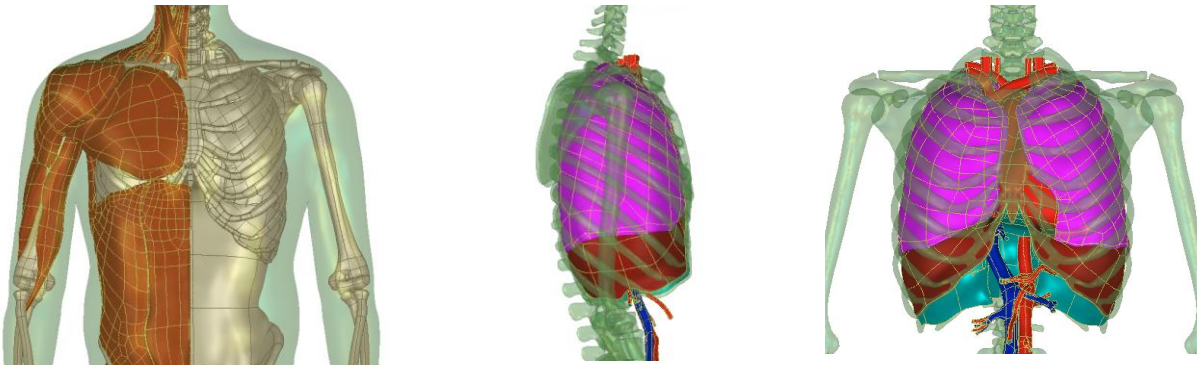

A B C

Figure 17: Views of 50th male CAD geometrical data. A. External view, transparent fascia, muscle groups and bone. B. Lateral view, transparent bone, right lung (pink) with diaphragm (maroon), C. Anterior view, transparent bone, lungs (pink), heart and great vessels (red), inferior vena cava (blue).

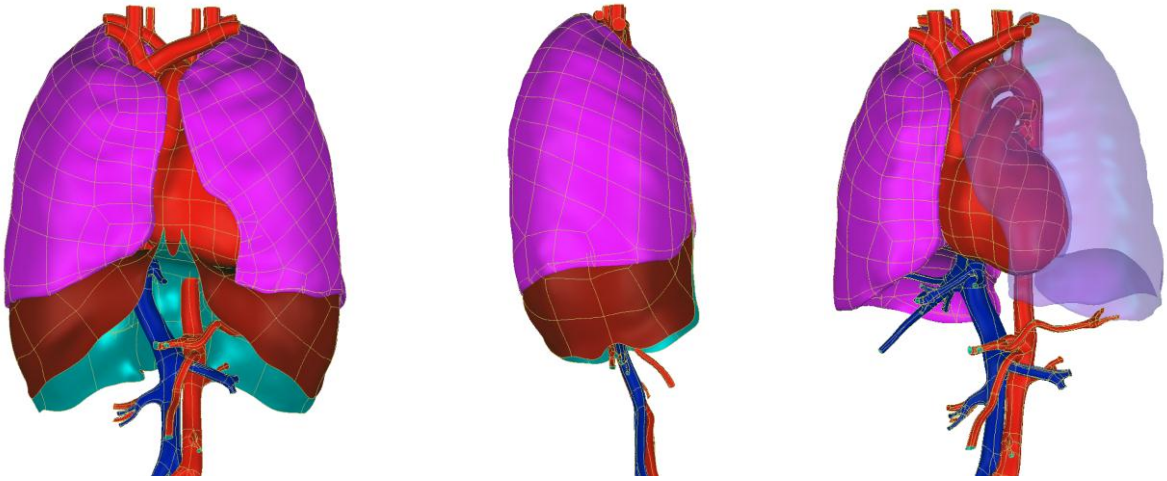

A B C

Figure 18: Views of interal organs of the thorax. A. Anterior view, heart, lungs, great vessels and diaphragm, B. Lateral view, lung, diaphragm, great vessels, C. Oblique view with left lung shown transparent. Isoparms of NURBS surfaces are visble.

This CAD data is intended for computational model analysis of blast or blunt injury. There are a number of advantages to this model development approach. Unlike other image datasets that rely on cadaveric data, nearly all soft tissue data in the average male model were derived from scans of a living subject. Unlike the data used in this study, none of the data sets commonly used in model development were acquired in the upright position, which greatly improves the geometrical accuracy of the model.

Injury Criteria

To develop lung injury criteria, real-world automotive crash cases will be modeled to correlate insult to outcome. Currently, all cases of interest have been pulled from the Crash Injury Research and Engineering Network (CIREN) database and the analysis of the extent of the pulmonary contusion and crash is complete. Work on modeling the crash is ongoing. This database was selected as the data source for this study because of the extensive medical data in

addition to the crash data. All cases selected have undergone a full case review with medical, engineering, and crash reconstruction specialists to determine injury causation. Additionally, these cases have medical imaging studies, in the form of DICOM data, uploaded to the database.

Subject Identification

The January 3rd, 2005 and January 3rd, 2011 CIREN data extracts, all case and complete case spreadsheets, were downloaded from the NASS Electronic Data System website on January 5th 2011. The "all" and "complete" case spreadsheets were both used to determine the cases selected. A case was selected for analysis is it met the following inclusion criteria: case year between 2005 and 2010, the presence of PC, a left or right side impact, impact on the same side as the occupant (a near-side impact), no rollover events, and a complete thorax CT available in the database.

Using the radiologic studies from CIREN case occupants, the percent volume of high radiopacity lung was quantified in Mimics (Materialise, Leuven, Belgium) using the method developed by the Virginia Tech / Wake Forest University Center for Injury Biomechanics and described by Weaver et al. (Weaver, Gayzik and Stitzel, 2009). This semi-automated method of segmentation relies on the difference in Hounsfield unit (HU) values between the air in the lungs and high radiopacity injured tissue. Uninjured tissue was clearly delineated with HU values between -1024 and -562 HU. Radiopaque tissue had a HU value greater than -562 and could be a variety of lung pathology including atelectasis, aspiration, or PC. Figure 19, Figure 20, and Figure 21 illustrate the lung as seen on medical imaging, a sample slice of a lung segmentation and the final three-dimensional reconstruction of the segmentation process. Figure 19 and Figure 21 show similar areas of high radiopacity lung tissue.

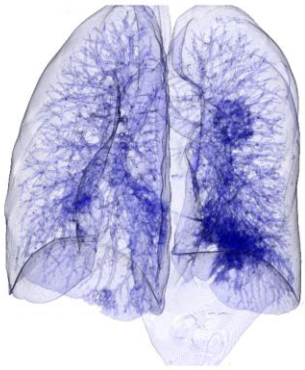

Figure 19: Three-dimensional reconstruction from medical images (oblique view) where the high radiopacity tissue is the darker areas within the lung.

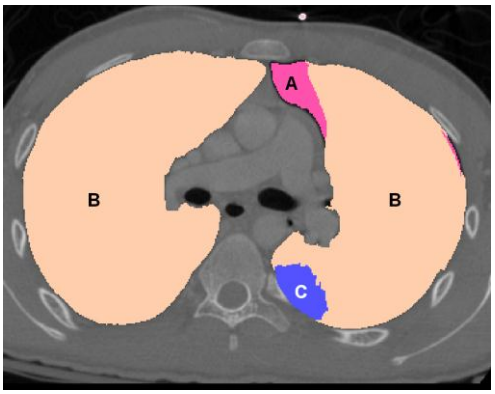

Figure 20: Sample segmentation of the lung tissue on one transverse slice of the CT scan. The area marked A is pneumothorax, B is the healthy lung area, and C is high radiopacity lung. The areas highlighted for C are also included in the total area for B.

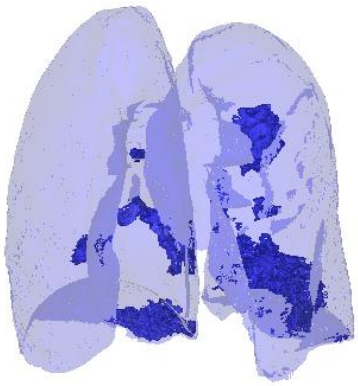

Figure 21: Three-dimensional reconstruction (oblique view) of the same segmentation as Figure 2 with areas of high radiopacity shown as darker areas within the lung.

The first step in this process was the selection of pneumothorax and trapped air, when present. This area was automatically selected based on the low Hounsfield unit value of air outside of tissue (HU values -1064 to -855). Next, all lung tissue was selected using the automatic thresholding command included in the software. A pixel with HU value of -562 was selected from the healthy lung tissue. This selection was expanded by including all touching pixels, starting from the original pixel, with a range of values from -452 to -352. Areas of pneumothorax and trapped air were subtracted from the total lung area. The total lung was manually adjusted to remove areas that were not lung parenchyma, such as large bronchioles and blood vessels at the lung hilum. Additionally, areas that were high radiopacity tissue within the lung were manually added into the total lung. During this phase of manual segmentation, fluid trapped outside of the lung but within the pleural space was not considered part of the total lung area. Next, the areas of high radiopacity lung were identified in a similar fashion, through automatic segmentation followed by manual editing. The automatic range for the high radiopacity lung was -562 to 3071. Areas of high radiopacity lung within the total lung area were selected then manually edited to remove blood vessels. The final result was three areas (total lung, healthy lung, and radiopaque lung) on each of the two-dimensional slices of the CT scan, Figure 20. The percent volume of PC was calculated based on the ratio of high radiopacity lung to total lung. These volumes can be three-dimensionally displayed, as shown in Figure 21.

Crash Parameter Selection and Calculation

All crash parameters were obtained from the CIREN database; however, the database was queried using two different methods. The first was by downloading the January 3rd, 2005 and 2011 data extracts as previously described. Not all of the crash parameters of interest were included in the data extracts; therefore, the other crash parameters were extracted from the database using the CIREN SQL interface and SQL developer (Oracle, Redwood Shores, CA). The data fields extracted from CIREN were: change in velocity (delta-V), Collision Deformation Code (CDC), average crush profile values (C1 to C6), average maximum crush, Field Length (Field-L), side airbags (SABs) present, vehicle type, occupant height and occupant age. The delta-V, as calculated from WinSmash, is a commonly selected metric to evaluate the severity of the crash. In the cases with no delta-V calculation available, the barrier estimate speed was used. The CDC is a seven digit alpha-numeric code that describes the area and extent of damage to the vehicle. Field-L is the distance from the first crush measurement (C1) to the last (C6).

The calculated parameters from the database fields are the area of crush and the location of the max crush relative to the occupant. Area of crush was based on the shape of the crush profile. The distance between the crush measurements was calculated by dividing the Field-L by 5. Then the area of the trapezoid formed by the two C-measurements and the distance between the measurements was calculated. This was repeated for each section of the crush profile and the sections summed to determine the area of the crush (Figure 22).

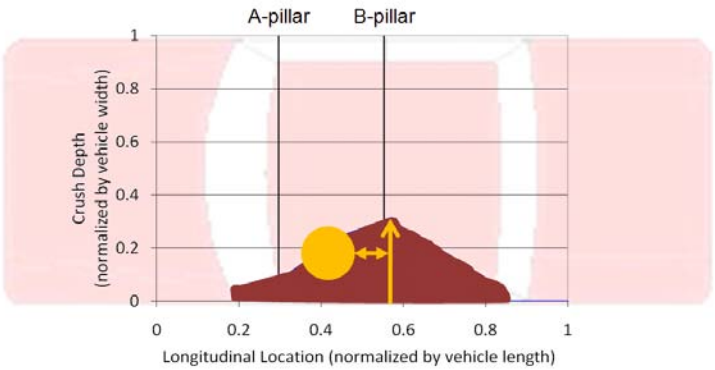

Figure 22: A sample illustration of the crush metrics. The occupant location is denoted with a grey circle. The black section is the area of the crush as defined by the crush profile data. The grey arrow with the single head is the measured maximum crush. The double headed arrow is the distance from the occupant to the maximum crush location.

In addition to calculating the area of the crush, the location of the lung in relation to the maximum crush was calculated (Figure 22). First, the lung height in relation to the vehicle frame of reference was determined. From an existing dataset of Faro arm measurements, point locations bounding the ribcage of six subjects, 3 male and 3 female, selected as representative of 5th, 50th and 95th individuals were recorded. From these data points, a linear regression of x- and z-axis location as a function of occupant height was calculated. The points used for this analysis were the suprasternal notch, the bottom of the sternum below the xiphoid process, the spinous process of C7 and the spinous process of T12 as shown in Figure 23 and Figure 24. The points were taken in a driving position and placed in the h-point coordinate system. Using the linear regression results, these point locations were calculated for all of the occupants in the study and the centroid of the occupant lung in the X-Z plane was selected as the occupant location point.

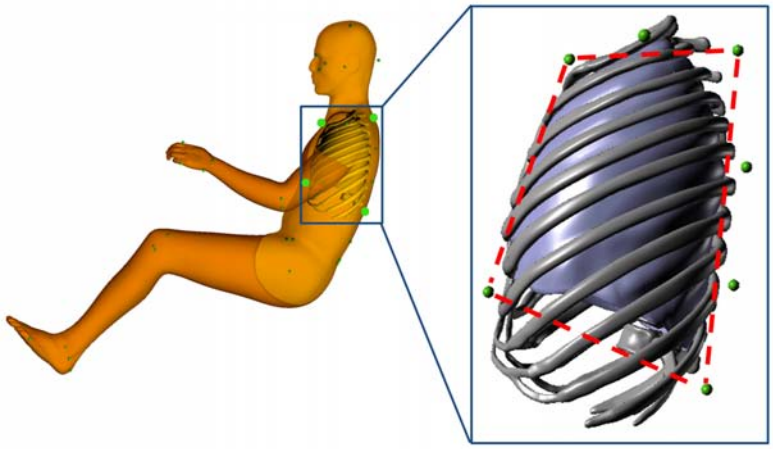

Figure 23: The location of the points selected to on a model of the average male. The inset box illustrates how these bony structure points bound the lung.

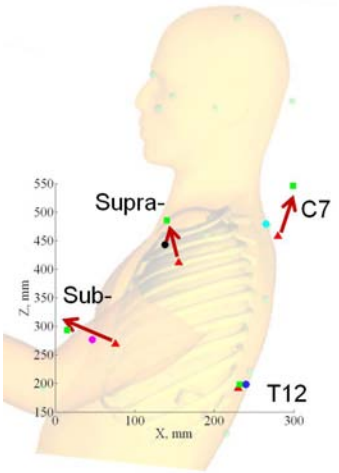

Figure 24: The point locations for the 5th (triangle), 50th (circle) and 95th (square) male subjects.

To determine the location of the maximum crush on the vehicle, vehicle test reports and measurements from crush profile pictures were used. For each vehicle, a vehicle test report was downloaded from the National Highway Traffic Safety Administration (NHTSA) Vehicle Crash Test Database. When the vehicle model or model year was not available an equivalent model or year was selected using the Sisters and Clones List (Anderson, 2008). The data recorded from the vehicle test report were: PHX and PHZ (distances from the occupant h-point to the b-pillar striker), level 1 (vertical distance from the ground to the sill), and level 2 (vertical distance from the ground to the h-point).

Given the relationship between the occupant h-point and the two visible components of the vehicle (sill and b-pillar), measurements from these components to the maximum crush location were related to the occupant h-point. For each case, the pictures that visualized the crushed side plane were selected. When possible the photograph that was perpendicular to the impacted surface was used for the photograph measurements. Using known distances, such as the alternating colors on the c-measurement sticks or the distance between measurements, a cm to pixel ratio was calculated for each picture (ImageJ, Bethesda, MD). Then, the maximum crush location was measured from the b-pillar and the sill. If the impact occurred on a location with a known measurement, such as on the b-pillar or at a scaled location, these known measurements were used instead of the picture measurement technique. Finally, the crush measurement was converted to an X- and Z-coordinate in the occupant h-point frame of reference. The Euclidean distance between maximum crush and the centroid of the lung was calculated and recorded as maximum crush distance from the occupant.

Side airbags deployment and occupant age are included in the analysis since they are postulated to be covariates in the relationship of crash severity and the extent of PC. An analysis of SABs from NASS was conducted to quantify this possible relationship. NASS data from 2000 to 2008 was downloaded from the NASS CDS FTP site accessed from the NHTSA Data webpage. Near-side cases with a delta-V close to NCAP testing speeds (43 to 63 kph) were selected for analysis. In cases without airbag deployment, the incidence of PC was 2.52%. In comparison, cases with airbag deployment had a PC rate of 2.22%, a 14% decrease. This difference is small; however, the deployment of a SAB was considered during this analysis.

Crash Analysis Results

For the 64 CIREN cases that meet the inclusion criteria for this study, 12 cases had SABs that deployed as a result of the crash. The individuals in the dataset tended to be younger, with 50 of the 64 individuals under the age of 55. The case Delta-V's covered a wide range of values; however, the majority fell below the range of the NCAP testing speeds (45/64 below 43 kph, with two cases missing a value).

Logistic regressions of Delta-V, average c-max, area of crush, and occupant distance from crush were performed to determine if there was a threshold at which these values would significantly predict a difference in the mean values of percent PC volume. For all variables except average c-max there was no significant value. For this one parameter, the value with the highest sensitivity and specificity was 50 cm of crush. The cases were grouped based on this finding and a one-way ANOVA of the groups was performed resulting in a mildly significant p-value of 0.072. The

mean PC percent volume for the group with an average c-max below 50 cm was 17.2 ± 11.7%. For the group with a c-max above this value, the mean was 24.5 ± 16.4%.

Next, Pearson correlation coefficients were calculated between the percent of PC and the variables of interest. Age and average c-max began to approach significance; therefore, these two variables were used in a multivariate regression to predict PC percent volume. The overall model achieved significance with a p-value of 0.033. The two independent variables were also significant predictors with p-values of 0.0305 for c-max and 0.0364 for age. Figure 25 plots the predicted versus the actual PC % volume based on this regression analysis.

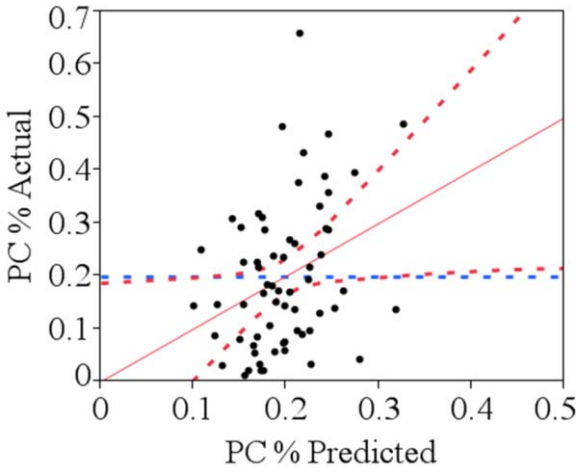

Figure 25: Predicted versus actual percent PC of the linear regression model.

Finally, age and SAB deployment effects were investigated separately. For the age grouping, the case occupants were separated based on the elderly classification for PC developed by Stitzel et al. (2010). These values were 58 years old for unilateral PC, 46 years old for bilateral PC, and 54 years old for PC not further specified. The first SAB group was occupants that had a SAB deploy as a result of the crash. The second group was occupants with no SAB present or SAB present but did not deploy. A one-way ANOVA found no significant difference between the groups.

Average maximum crush was selected as a measure of door intrusion and was the one crash parameter shown to have statistical significance. This variable has been show to correlate to the incidence of PC in previous studies (Tencer, Kaufman, Mack et al., 2005). Intrusions into the occupant compartment in a pole impact have been shown to cause antero-lateral loading of the chest resulting in frequent unilateral chest injuries, including PC (Pintar, Maiman and Yoganandan, 2007). The Pintar (2007) study also demonstrated that the proximity of the occupant relative to crush was correlated to a high rate of thoracic trauma in side pole crashes.

Age, as part of a multivariate regression, was also a significant predictor for PC. As mentioned previously, Stitzel et al. (2010) identified age thresholds associated with increased mortality of PC. Other studies have also demonstrated the increased likelihood of injuries in older individuals (Kent, Trowbridge, Lopez-Valdes et al., 2009). There is also evidence that older individuals have a different ribcage geometry (Gayzik, Yu, Danelson et al., 2008) and bone material properties (Burstein, Reilly and Martens, 1976; Zioupos and Currey, 1998).

One limitation of the study is the identification of PC on CT scan. Atelectasis and aspiration both appear as high radiopacity tissue within the lung with the same HU values as PC. To adjust for this, the scans were reviewed by an expert in thoracic imaging. After this review, it was noted that while some individuals had areas that could not be positively identified as PC, the majority of individuals had radiologic evidence that the high radiopacity tissue was PC. The evidence considered in identification of PC were the presence of pneumatoceles, radiopaque tissue near rib fractures, radiopaque tissue that crossed lobe lines, and radiopaque tissue along the periphery of lung or in the apical regions (Wagner, Crawford and Schimpf, 1988).

The manual component of the segmentation process had the potential to introduce variability in the volume data. For this analysis, there were three individuals that conducted all segmentation. Two researchers completed 58 of the scans and one researcher completed six scans; however, the same individual checked and modified all completed segmentations prior to volume data collection. Therefore, within this dataset there is limited inter-observer variability. An intra-observer study was conducted with three scans repeated after a time interval of two weeks. The results demonstrated that the selection of the higher radiopacity tissue demonstrated more variability than the total lung area. The difference between the total lung volumes, expressed as a percentage of the first lung segmentation volume, was 1.7 ± 2.5%. The variability in high radiopacity tissue, again as a percent of total lung volume, was 4.3 ± 1.6%.

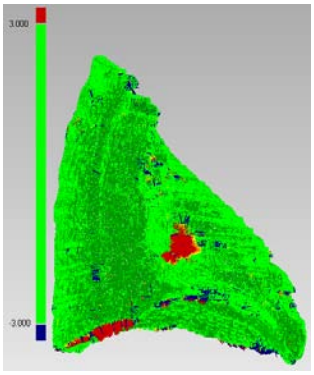

Figure 26: Deviation between a segmented lobe and a lung atlas lobe after a surface registration algorithm was completed. The areas in green are where the deviation between the two images was within the resolution of the CT scan. The red and blue sections have variations beyond this threshold.

Future work will determine the location of PC in these patients using a lung atlas for co-registration. To put the segmented trauma scans in the same coordinate system as the atlas, rigid and affine registration transformations will be used to morph the trauma scan to the atlas space. This morphing will allow for a better comparison of lesion location between different individuals in the study. Initial work is complete on a method to register the segmented pulmonary contusion to a lung atlas. Figure 26 shows the deviation between a segmented lobe and a lung atlas lobe after a surface registration algorithm was completed. The areas in green are where the deviation between the two images was within the resolution of the CT scan. The red and blue sections have variations beyond this threshold. Future work will continue to improve the registration procedure.

References

Anderson GC. Vehicle Year & Model Interchange List (Sisters & Clones), Madison, WI, 2008.

Burstein AH, Reilly DT, Martens M. Aging of bone tissue: mechanical properties. J Bone Joint Surg Am 58(1): 82-6, 1976.

Gayzik FS, Yu MM, Danelson KA, et al. Quantification of age-related shape change of the human rib cage through geometric morphometrics. J Biomech 41(7): 1545-54, 2008.

Kent R, Trowbridge M, Lopez-Valdes FJ, et al. How many people are injured and killed as a result of aging? Frailty, fragility, and the elderly risk-exposure tradeoff assessed via a risk saturation model. Ann Adv Automot Med 53: 41-50, 2009.

Pintar FA, Maiman DJ, Yoganandan N. Injury patterns in side pole crashes. Annu Proc Assoc Adv Automot Med 51: 419-33, 2007.

Tencer AF, Kaufman R, Mack C, et al. Factors affecting pelvic and thoracic forces in near-side impact crashes: a study of US-NCAP, NASS, and CIREN data. Accid Anal Prev 37(2): 287-93, 2005.

Wagner RB, Crawford WO, Jr., Schimpf PP. Classification of parenchymal injuries of the lung. Radiology 167(1): 77-82, 1988.

Weaver AA, Gayzik FS, Stitzel JD. Biomechanical analysis of pulmonary contusion in motor vehicle crash victims: a crash injury research and engineering network (ciren) study - biomed 2009. Biomed Sci Instrum 45: 364-9, 2009.

Zioupos P, Currey JD. Changes in the stiffness, strength, and toughness of human cortical bone with age. Bone 22(1): 57-66, 1998.

Task 3.2: Physical Lung Model: Pulmonary Surrogate Development

Based on discussions with USAARL, the development of a physical lung model (pulmonary surrogate, task 3.2) has been substituted with an effort to develop a head surrogate for free field blast testing. The head form is intended as a platform for blast injury prediction of the eye as well as the brain. In both cases, experimental data obtained from tests will be paired with computational modeling efforts. Results of the development of these tools are presented here.

The purpose of the free field head surrogate is twofold. The first is a broad aim to acquire pressure profiles on the anterior aspect of the face from incident blast waves in live fire testing. The second, more focused aim is to collect incident pressure data on an instrumented eye surrogate that will be embedded into the head surrogate. Regarding the first aim, incident pressure on the ventral surfaces of the surrogate will be used to validate boundary conditions for computational modeling of the head in subsequent efforts. Regarding the second, the eye surrogate itself will be instrumented with an internal pressure sensor and has been sized to match an existing FEA model of the eye developed at Virginia Tech.

This section discusses initial the development efforts to date on the physical model of the skull, and surrounding fascia that comprise the head form. Following this, data on the development of the eye surrogate is presented. For the skull and fascia, a representative 50th percentile male subject was scanned using a clinical scanning protocol. The skull, and fascia components were conditioned for rapid prototyping with additional mechanical connections for base structure and sensor attachment.

Subject Recruitment and Imaging Data for the Head Surrogate

A 50th percentile male volunteer (26 y, 78.6 kg, 174.9 cm) was selected to be the basis for model development. The subject met criteria for external anthropometry based on ANSUR data (Gordon, Churchill et al. 1989) for the average male. By utilizing data that has been sized to the average male from a study of service members, the model development will result in a tool that will have broad applicability moving forward. The same imaging protocol described in Task 2.1 on the development of the Neck CAD data was applied to acquire the images used in this phase of the work. Specifically, CT data was used on this aspect of the project. A pre-programmed bone kernel was used in CT image reconstruction to facilitate segmentation of the skull. The resulting image resolution for the head region was 0.50 mm in-plane resolution with 0.63 mm thickness.

Segmentation of the Skull and Facial Tissues

Skull and fascia geometry was created using a commercial segmentation and image analysis program (Mimics, Materialize Inc., Leuven, Belgium). The visualization of these masks below was completed using Tera Recon's AquariusNet Viewer, v.4. The segmentation process is shown in Figure 27. The exterior and interior boundaries of skull and mandible were isolated using thresholding segmentation based on Hounsfield unit values greater than 260 HU. External facial features were then segmented using a similar approach. Initial segmented surfaces were exported as polygonal surface data for further conditioning.

A. B. C.

Figure 27: CT image of skull from average male subject. A. Skull mask shown beneath rendered facial tissue. B. Anterior view of skull bone mask, C. Lateral view. This data is non symmetric and raw (rendered directly from images). The rapid prototyped surrogate geometry has had symmetry enforced.

Conditioning and Rapid Prototyping of the Segmented Data

An additive manufacturing solution is required to produce the complex geometry of the skull. Prior to prototyping, a number of conditioning operations were applied. Segmented data were conditioned to enforce mid-sagittal symmetry. Additional conditioning was applied to remove image artifacts from segmentation, and to remove small features and holes in preparation for fabrication. The mandible was structurally attached to the skull via added connections. Rear portions of the skull were removed for access to the inner cavity. This is space was designed to house wires from instrumentation that will be mounted from the rear of the surrogate but will face the ventral aspect. Simplifications of the atlanto-occipital joint were completed and a mechanical connection inserted for future fixation of in tests, see Figure 28. Boolean operations were conducted using the exterior facial surface and skull geometry to develop a variable thickness component representing external fascia, panel C below. Further conditioning was applied to the fascia geometry to eliminate facial recognition to the original recruited subject. All components were transformed to a common coordinate system (SAE J1733) with the Frankfurt plane of the positioned head parallel to XY axis.

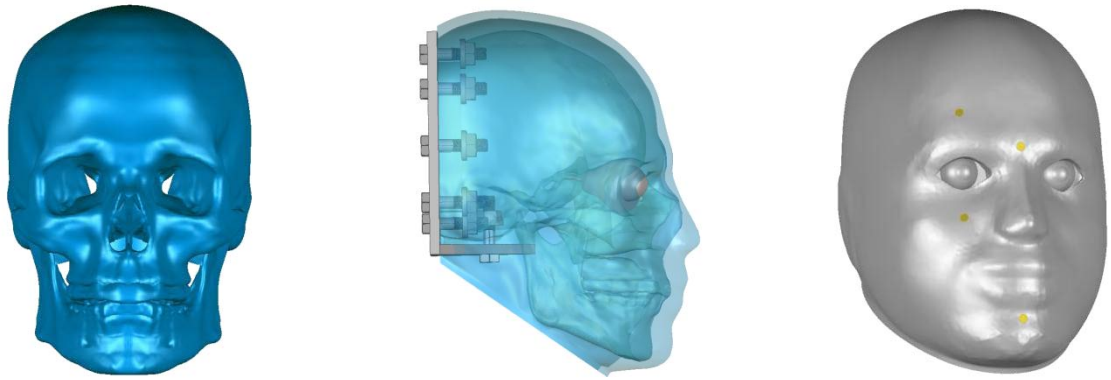

A. B. C.

Figure 28: A. Frontal view of skull surrogate design, B. Lateral view of skull surrogate design with back plate, transparent fascia, and eye surrogate, C. Oblique frontal view with fascia, eyes and integrated sensors (gold marks).

While the head surrogate was designed to acquire pressure profiles on the face in a blast environment, it will also serve as a realistic housing for the eye surrogate currently under development. Below, the eye surrogate development is discussed in greater detail. The placement of the eye surrogate within the head surrogate is shown in Figure 3. Figure 3B shows a cut away view of the head surrogate. The striped areas signify rapid prototyping material fill. This area is actually more complex in the skull with thin layers of cortical bone around softer cancellous bone, or open cavities of air that are the sinuses. These features were removed for added strength of the surrogate without disrobing to design on the ventral aspect. The turquoise blue is in the inner portion of the skull cavity. The gold color cutaway shows the external fascia layer.

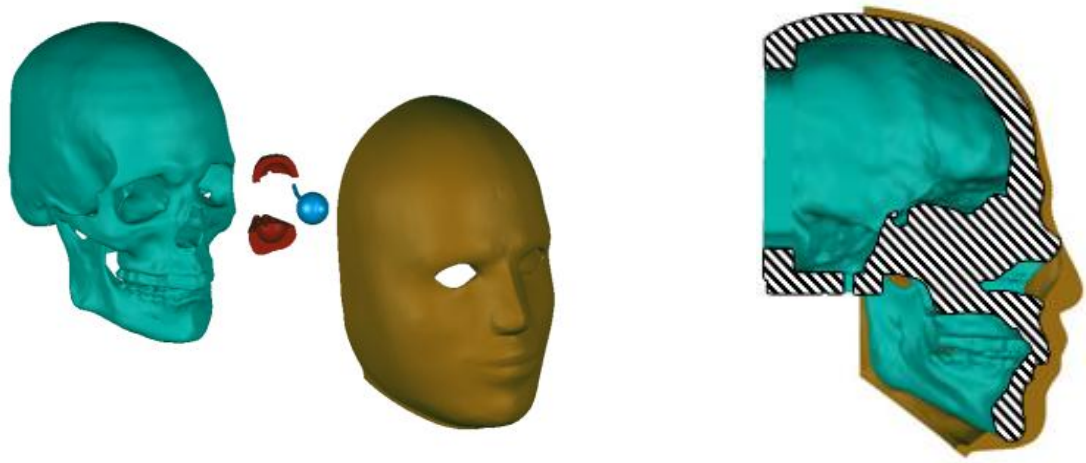

A. B.

Figure 29: A. Symmetric skull, right eye, surrounding tissue, and frontal fascia (also symmetric). B. Cut away view of skull and fascia.

Prototyping Process Selection

Selective Laser Sintering (SLS) was chosen to produce the functional and structural bony tissue geometry for the physical model. SLS is an additive rapid prototyping process that builds three dimensional parts by using a laser to fuse powered material. This enables complex, organic geometry to be created with high accuracy and be used as functional test fixture. The conditioned polygonal objects from segmentations feed directly into the 3rd party SLS development process for creation of 3D anatomic structures.

Silicon molds were also designed and developed to create a cast urethane model of the variable thickness fascia component. Due to the size, complex concavity and required physical properties, the cast component was chosen over a more costly rapid prototyping process. The fascia molds will also be reusable for testing different types of elastomeric urethanes in a more cost effective manner. The design of the mold is shown in Figure 4.

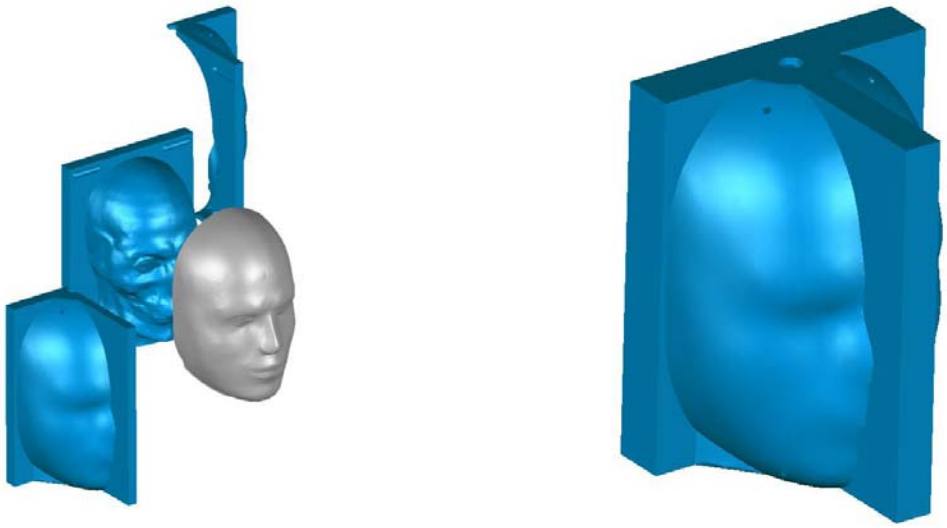

Figure 30: Mold design for casting the frontal fascia of the head surrogate. The molds will be rapid prototyped. Elastomeric urethanes of various properties will be used to fabricate this component so that materials of various stiffnesses can be tested on the surrogate skull.

Material Selection for Test Surrogate

Nylon 12 PA (unfilled polyamide) and Nylon 12 GF (glass filled) were chosen for rapid prototyping bone material using the SLS processes. The materials provide a high strength (tensile: 40-45 MPa; flexural: 1,240-2,200 MPa) and durability to weight (1.0-1.4 g/cc). A number of elastomeric urethanes will be tested for the face material, from Shore A hardness 15 to 60. These encompass various material properties including elongation from 300%-1100% and tensile strength 1.65 -5.07 MPa. Data from the literature can be used to assess how realistic the chosen material behaves. One example of this is shown in Figure 31, where data from a quasi-static elongation of Tango Plus material is plotted next to data on an equivalent test from the literature (Yamada [illegible] on the CIB's MTS machines.

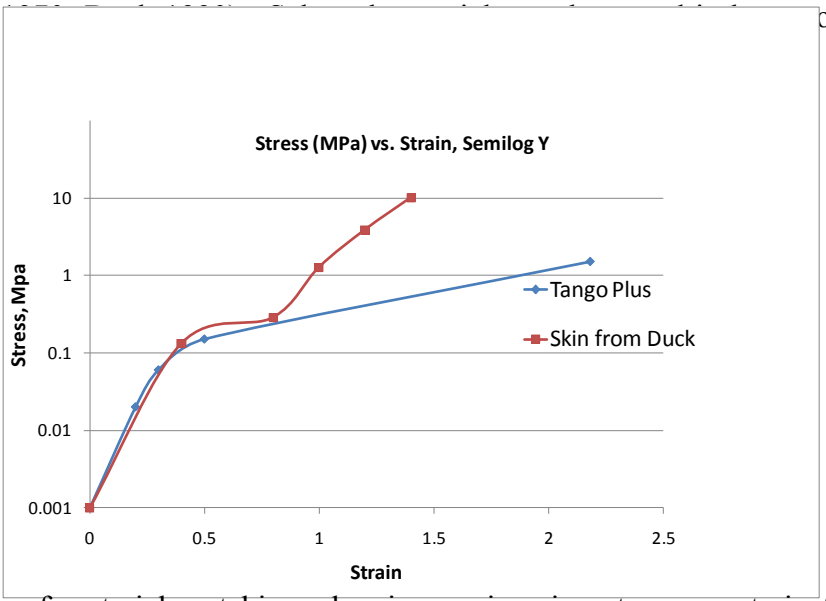

Figure 31: Example of material matching, showing engineering stress vs. strain for skin and rapid prototype material (Tango Plus) (Duck 1990).

Sensor Selection for the Head Surrogate

Sensors locations are to be built-into the fixture using mechanical fasteners or prototyped directly into the skull material, see Figure 28. Miniature pressure transducers from Kulite and PCB have been selected, see Figure 32. The Kulite XTL-140 (M) series was chosen for its compact exterior thread dimension (6-32 NC-2A) design and its high natural frequency (150-700 Hz). It is available with pressure ranges 5 to 500 psi respectively. The final selection for this transducer has a max pressure reading of 250 psi. The transducers will be customized for blast application with the inclusion of a potting material on the leading edge to improve response and provide protection for the sensing elements. The PCB blast transducer 113B21, with 200 psi pressure ranges and <1.0 μs rise time were also selected for their role in blast measurement. They incorporate an external thread (1/4-24?) with a small form factor. The PCB transducers require a 4-channel ICP sensor signal conditioner. A PCB free-field blast pressure sensor, model 137A24, pencil probe was also purchased for free-air pressure measurement with a range of 250 psi.

A. B. C.

Figure 32: Sensors for use in head surrogate. A. Kulite XTL-140 (M), B. PCB 113B21, C. PCB 137A24 pencil probe for free field blast testing.

Method for the Creation of a Rapid Prototyped Surrogate Eye

The Center has also applied this design paradigm to eye injury. The eye rupture prediction prototype was created in conjunction with an FEA model to predict eye injury and rupture. This model was created from average geometric measurements found in literature of the sclera and cornea along with mechanical property data obtained from material testing.

The eye surrogate is a single closed compartment with an internal pressure transducer to measure inner ocular pressure (Figure 33). This measure can then be correlated with risk of eye rupture. Computational models, can be used to augment these findings as well (Stitzel and al. 2002). Like the lung and head surrogate, it is produced through rapid prototyping and is composed of a digital composite material to best match physiologic mechanical properties of the eye. The eye surrogate is currently being investigated for use with the head form described above and other existing head forms. The eye surrogate is shown in Figure 34, with the detachable retinal interface for pressure sensing equipment. A cutaway view is shown to demonstrate the interior of the model.

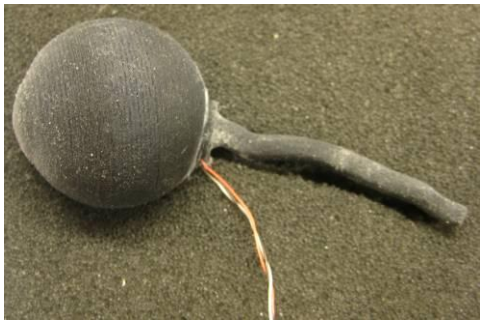

Figure 33: Rapid prototype synthetic eye model.

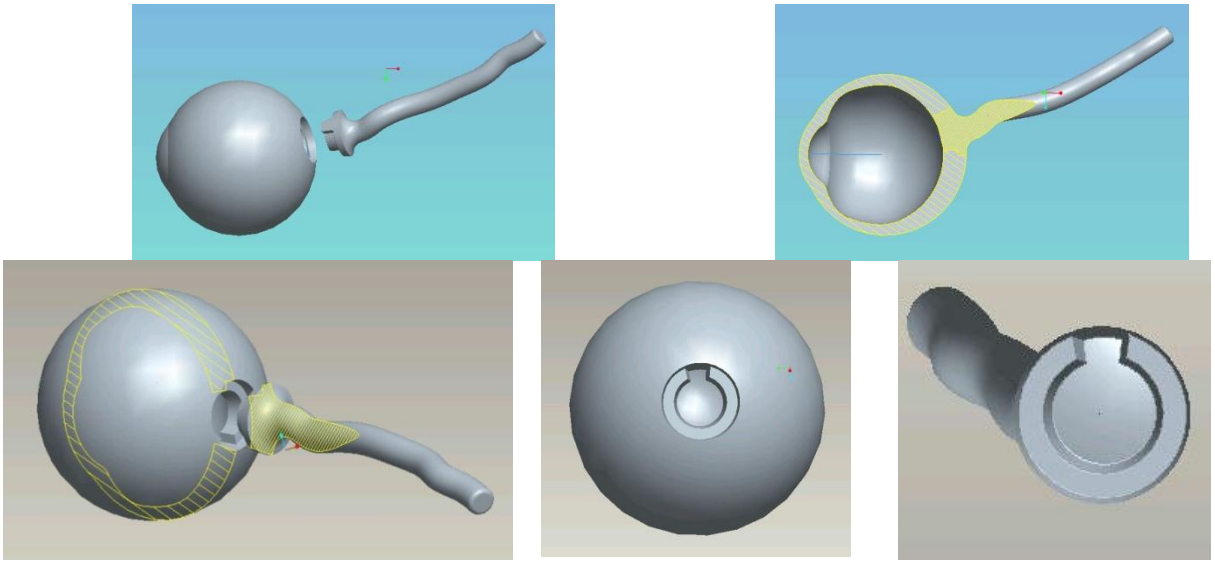

Figure 34: Single compartment Eye Rupture Surrogate. Various views. Clockwise from top left; detachable retinal interface, cutaway view, anterior view retinal attachment, posterior view eye, posterior-oblique view showing midplane.

Model dimensions match literature studies for diameter, thickness, volume, and morphology. The eye geometry was created based on the dimensional thicknesses of the sclera and cornea found in Stitzel et al's paper entitled "A Nonlinear Finite Element Model of the Eye with Experimental Validation for the Prediction of Globe Rupture" (Stitzel and al. 2002). Several other ophthalmology references were also used to augment this data (Spalton, Hitchings et al. 1994; Spencer 1985; Snell and Lemp 1998). A commercially available modeling package (Pro-E, v. Wildfire 2.0 by PTC) was used to create the parts and STLs for rapid prototyping. A cross-sectional drawing of the eye surrogate design is shown below in Figure 35.

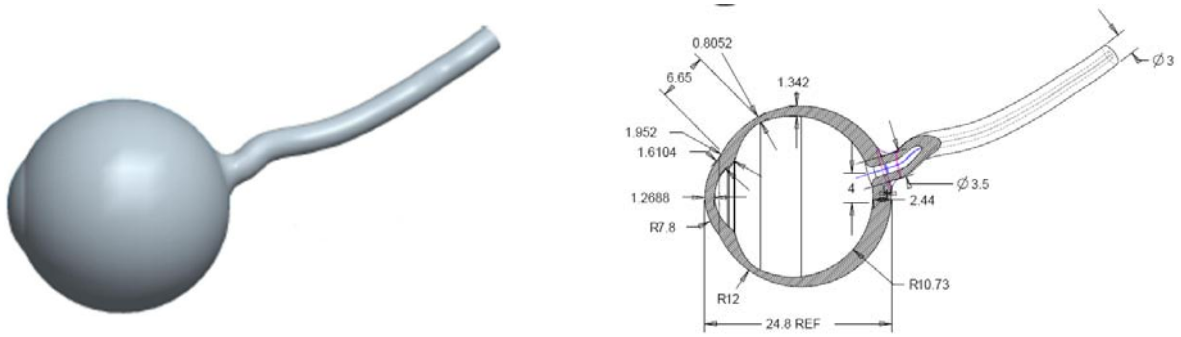

Figure 35: Engineering design drawings for CAD rendering of the eye used to develop the eye surrogate, dimensions in mm. Not to scale.

The elastic properties of the sclera and cornea were also obtained from Stitzel et al, 2002. While the elastic properties of these materials are nonlinear, to simplify the material matching task, we only used the first linear portion of the stress strain curve to determine the young's modulus of elasticity. The elasticity of the cornea and sclera were assumed to be 130MPa and 325MPa. The tensile stress of the eye at rupture is reported by to be 23MPa (Stitzel et al, 2002).

We compared the eye properties to the Objet rapid prototyping material properties that are currently available from our vendor. This comparison can be seen in Figure 36 below. The two materials that were found to best match the eye properties were the rubber material named "Tango Grey" and a plastic material named "Vero White". Both of which were an order of magnitude off of the target elasticity (one higher, one lower), had higher tensile strengths, and strain at failure than the cornea and sclera. These materials were used for initial fabrication.

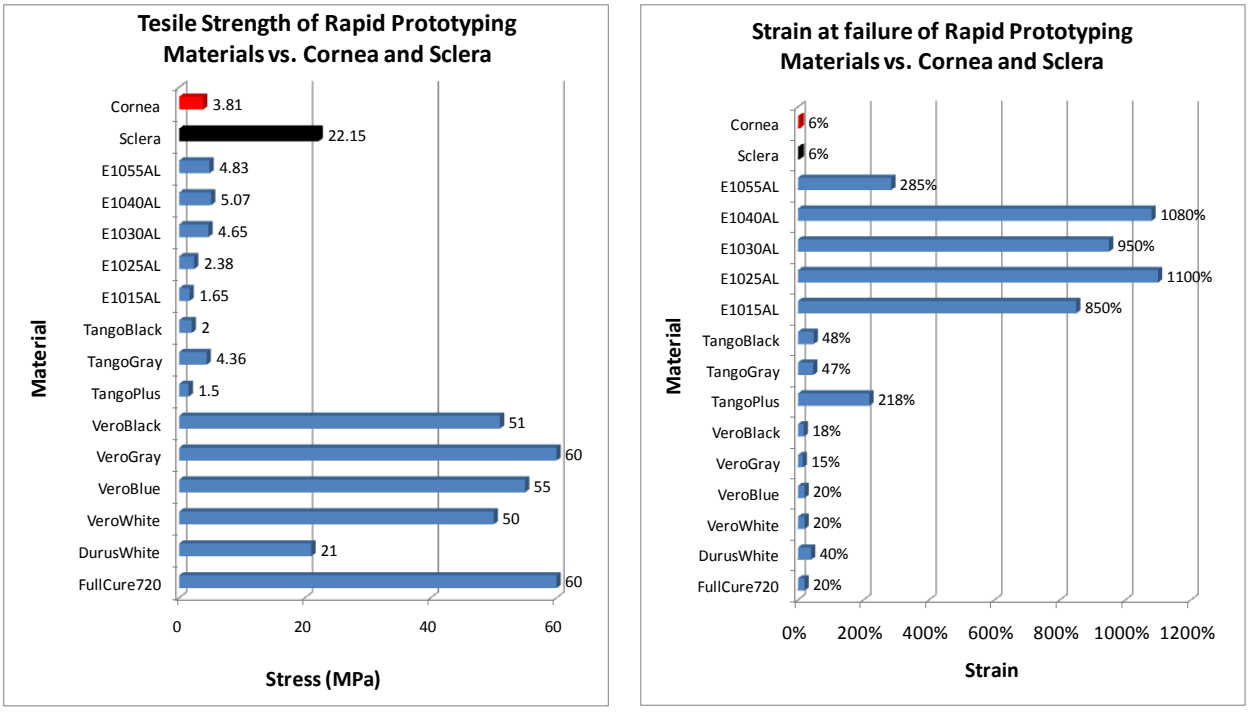

Figure 36: Comparative study of materials for eye surrogate prototype.

Durability of the surrogate eye is important, and for that reason a hybrid material composed of Tango Black Plus and Vero White (DM_9860 from Objet) was ultimately selected after a number of trials. In order to compensate for the more elastic rubber, the wall thickness of the surrogate eye was thickened to provide the same displacement under a similar axial load. To do this, a load cell ring displacement formula was used (Equation 1), and all variables were assumed to be equal except for the young's modulus and thickness (Equation 2). The newly acquired thickness (Equation 3) could then be used as a ratio and applied to the CAD eye model.

$$\partial = \frac{P * R^3}{E * w * t^3} \qquad \text{Equation 1}$$

$$E_1 * {t_1}^3 = E_2 * {t_2}^3 \qquad \text{Equation 2}$$

$$t_2 = \sqrt[3]{\frac{E_1 * {t_1}^3}{E_2}} \qquad \text{Equation 3}$$

Using the above approach, we calculated a thickness ratio for the cornea and the sclera and applied this to the appropriate sections of the inner eye surface of the surrogate. This allows the external dimensions of the eye to remain identical to anatomical measurements. To model the optic nerve the trajectory path was obtained through the 50th male MRI dataset (Gayzik, Hamilton et al. 2009). A spline was created and exported into Studio software (v. 12, Geomagic, Research Triangle Park, NC) where the coordinate system was translated into the eye geometry coordinate system. The spline was then used to create the nerve geometry.

In order to print the eye model, it was necessary to engineer an opening into the geometry to remove the support structure that existed within the eye as a consequence of the rapid prototyping process. To accommodate this opening, we chose to turn the optic nerve insertion into a plug so that the main portion of the eye would be a single continuous piece. This also allows for easier insertion of the internal eye pressure sensor. The sensor can be inserted from the inside outward, threading the sensor wire from the inside of the plug and out of the nerve (See Figure 33).

The final surrogate is a single compartment eye that does not include the lens, ciliary body, or iris. A second model of the eye that includes these structures has been created and contains two compartments. We are currently developing methods to rapid prototype this two-compartment model.

References

Duck, F. (1990). Physical Properties of Tissue, A comprehensive reference book. London, Academic Press.

Gayzik, F., C. Hamilton, et al. (2009). Multi-Modality Image Data Collection Protocol for Full Body Finite Element Model Development. SAE Digital Human Modeling. Gothenburg, Sweden, SAE.

Gordon, C., T. Churchill, et al. (1989). 1988 Anthropometric Survey of U.S. Army Personnel: Methods and Summary Statistics. D. a. E. C. Prepared for United States Army Natick Research.

Snell, R. and M. Lemp (1998). Clinical Anatomy of the Eye. New York, Wiley Blackwell.
Spalton, D. J., R. Hitchings, et al. (1994). Atlas of clinical ophthalmology. London, Mosby-Year Book Europe Limiated.
Spencer (1985). Ophthalmic Pathology: An Atlas and Textbook. Philadelphia, Suanders Company.
Stitzel, J. D. and e. al. (2002). "A Nonlinear Finite Element Model of the Eye with Experimental Validation for the Prediction of Globe Rupture." Stapp Car Crash J.
Yamada, H. (1970). Strength of Biological Materials. Baltimore, Williams and Wilkins Company.

Task 3.3: Thorax Protection: Crash System Development

Specific Objective of Task 3.3:

1. Develop and obtain a custom mechanical sled crash system capable of recreating a wide range of crash impact scenarios

A tremendous amount of time was spent on the installation and initial validation of the new servo-hydraulic sled system. The 1.4 MN Seattle Safety System was installed and initial tests were performed to verify the accuracy of the sled pulse. Table 1 displays specifications for the sled system. Similar to pin/orifice-based sled systems, the ServoSled uses a high pressure pneumatic actuator to apply force and energy to the sled. A hydraulic friction "servobrake" acts directly on the sled to oppose the actuator force thus controlling the net force and energy put into the sled. The servobrake pressure is varied during the test pulse by high-speed computer-controlled servo-valves to absorb "excess" actuator energy – energy above that required for the pulse. Following a pulse, the sled rolls away from the actuator ram at constant velocity while the ram is stopped by a low-pressure air cushion. There are no restrictive flow devices within the actuator as all pulse control is by the servobrake and computer control system. A range of acceleration profiles have been performed ranging from 2.5g, to 30g, to 60 peak acceleration pulses. In all cases the system has performed very well and is extremely repeatable. Furthermore, the system was able to go from a 2.5g peak acceleration pulse to 30g peak acceleration pulse with only 30 minutes of change time in between. This will be useful as we explore low and high severity tests on the same PMHS.

Table 1: Specifications for the 1.4 MN ServoSled.

	1.4 MN ServoSled
Nominal Force	1400 KN *(315,000 lbf)*
Available Stroke	2000 mm *(79 in)*
Maximum Velocity	90 kph *(56 mph)*
Peak Acceleration (at 250kg payload)	93 g
Maximum Jerk	20 g/msec
Maximum Payload	2500 kg *(5500 lb)*
Maximum Energy	475,000 N-m *(350,000 ft-lbf)*
Sled Dimensions	3.0m L x 1.5m W *(118" L x 59" W)*

Additionally, work has continued on the integration of sled support systems, such as: data acquisition, video, lighting, and the VICON motion analysis system. A custom lighting system was designed, manufactured, and installed for the sled impact area. The design includes top, side, back, and front lighting mounts relative to the initial buck position. The frame holds 90 high-frequency fluorescent lights, giving a total output of 1.1 million lumens. The frame hangs from the ceiling with a winch system that can lower the entire frame from a height of 13 feet to 4 feet above the floor depending on the requirements of any future work. The setup provides very even light with no hotspots or shadows by surrounding the initial buck position on all sides. In addition, the lighting system only uses 30% of the amount of power of an equivalent tungsten filament lamp. Figure 37 displays various views of the completed lighting system mounted above the sled.

Figure 37: Various views of the lighting system mounted above the sled system.

Furthermore, additional low and high severity pulses were performed in order to evaluate the abilities of the sled system. The system was able to go from a 2.5g peak acceleration pulse to 30g peak acceleration pulse with only 30 minutes of change time in between. This will be useful as we explore low and high severity tests on the same PMHS.

Task 4.1: Military Biomechanics: National Research Symposium

Specific Objective of Task 4.1:

1. Host and sponsor a national injury biomechanics symposium specifically for military applications. The focus of this task will be to educate doctors, engineers, and others in injury biomechanics, in particular for these body regions, but also to include other at-risk areas. There will be guest lecturers as well as invitations to all scientists in this field. These symposiums will correspond to each phase of this research proposal to encourage biomechanics information dissemination that is targeted to military personnel but open to civilians.

The first Military Biomechanics Symposium was successfully held on August 4th and 5th of 2009 in Washington DC (Figure 38). A total of 130 people attended 20 lectures covering advances in injury biomechanics and an overview of blast physics with applications. This forum allowed for interactions and collaborative discussions that will lead to new partnerships and ultimately better protection for soldiers. The success of this symposium highlights the importance of these symposiums to assist in the translation of the research to practice.

Figure 38: 130 people attended 20 lectures for the first Military Biomechanics Symposium.

The following 3 pages display the agenda and lecture content of the Military Biomechanics Symposium.

Advanced Technologies and New Frontiers in

Injury Biomechanics

With Military and Aerospace Applications

Program Guide

August 4th 2009: 8:30 am – 5:00 pm

Advances in Injury Biomechanics

August 5th 2009: 8:30 am – 5:00 pm

Overview of Blast Physics and Applications

Doubletree Hotel Crystal City

Arlington VA, Between the Pentagon and National Airport at Washington DC

Sponsored by:

DTS

DENTON

Virginia Tech CIB Wake Forest

Center for Injury Biomechanics

CFDRC

: Tuesday, August 4th 8:30 am to 5:00 pm

vances in Injury Biomechanics

The course content is based on real-world crash analysis, case studies, experiments with human and dummy surrogates, and computer models. A combination of slides, movies, and demonstrations will be used to cover the following topics:

gistration and Continental Breakfast *(provided)*
roduction and Overview
Stefan Duma, Virginia Tech

ad Injury Biomechanics
strumented Helmet Data Collection and Analysis"
Steve Rowson, Virginia Tech
igh Speed X-ray of Human Head Impact Biomechanics"
Warren Hardy, Virginia Tech
)CUS Headform and Facial Fractures"
Joe Cormier, Biodynamic Research Corporation

ffee Break ***(refreshments provided)***

ck and Thorax Injury Biomechanics
ead Supported Mass Injury Risk and Biomechanical Evaluation"
Carol Chancy, United States Army Aeromedical Research Laboratory
ultiscale Characterization of Human Bone and Soft Tissues"
Andrew Kemper, Virginia Tech
ıng Injury Experimental and Modeling Biomechanics"
Scott Gayzik, Wake Forest University

ıch ***(provided)***

torcycles and Military Vehicles
otorcycle Crashes: Fatality Risk, Guardrail Impact, and Training Effectiveness"
H. Clay Gabler, Virginia Tech
aturalistic Motorcyle Instrumentation, Data Collection, and Analysis"
Zac Doerzaph, Virginia Tech Transportation Institute
-depth Military Helicopter Accident Investigations"
Joe McEntire, United States Army Aeromedical Research Laboratory
REN Capabilities and Military Applications"
Joel Stitzel, Wake Forest University

ffee Break ***(refreshments provided)***

SA and Advanced Modeling
verview of ORION Constellation Program and Crew Injury Prediction"
Jeff Jones, NASA
valuation of NASA Suit Interface and Landing Conditions"
Kerry Danelson, Wake Forest University
lodeling Human Variation: Orbit Anthropometry and Effect on Eye Injury Metrics"
Ashley Weaver, Wake Forest University
euroscience, Imaging, and Health Informatics at Virginia Tech"
Kenneth Wong, Virginia Tech

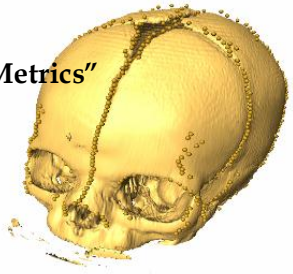

journ

Wednesday, August 5th 8:30 am to 5:00 pm

rview of Blast Physics and Applications

istration and Continental Breakfast *(provided)*

oduction and Overview
oel Stitzel, Wake Forest University

ion 1: Blast Physics
Charles Needham, Principal Physicist, Applied Research Associates Inc.

- **Basic Airblast Definitions**
- **Conservation Laws and Rankine-Hugoniot Relations**
- **Propagation Geometry**
- **Detonation**
- **Explosive Characteristics**

ee Break ***(refreshments provided)***

ion 2: Blast Applications
CUS Response to Blast Loading"
Fred Brozoski, United States Army Aeromedical Research Laboratory

ree-Dimensional Computational Modeling of Blast Loading"
Andrzej Pzekwas, Computational Fluid Dynamic Research Corporation

st, Present, and Future Dummy Development and Data Acquisition in the Military"
Mike Beebe, Denton Inc, and Mr. Steve Moss, DTS Inc.

ch ***(provided)***

sion 3: Blast Physics Continued
Charles Needham, Principal Physicist, Applied Research Associates Inc.

- **Burn Models**
- **Interaction and Multiple Detonation**
- **Case Expansion and Fragmentation**
- **Air Shock Formation**

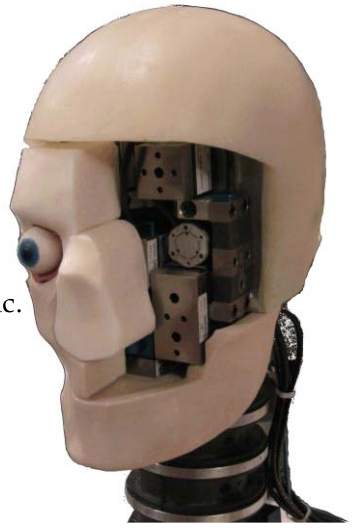

ee Break ***(refreshments provided)***

ion 4: Blast Physics Continued
Charles Needham, Principal Physicist, Applied Research Associates Inc.

- **Simple Scaling, Simple Reflection, Mach Reflection**
- **Structure Interactions**
- **Introduction to Instabilities**

burn